



Characterisation of the wake of the DrivAer estate vehicle[☆]

T. Avadiar^{*}, M.C. Thompson, J. Sheridan, D. Burton^{**}

Department of Mechanical and Aerospace Engineering, Monash University, Melbourne, 3800, Australia



ARTICLE INFO

Keywords:

Automotive aerodynamics
Wind tunnel
Bluff body
Wake

ABSTRACT

To date, little information has been published on the time-averaged wake of the *estate* variant of the *DrivAer* vehicle type. In recent years, this generic automobile geometry has been put forward as a more realistic alternative to investigate vehicle aerodynamics than considerably more idealised geometries, such as the *Ahmed body*. In this paper, the time-averaged wake is experimentally investigated through wind-tunnel tests. Velocities maps and profiles, drag-force measurements and base pressure distributions are used to characterise and quantify the flow behind and around the vehicle. In particular, the combination of wake-velocity and base-pressure measurements provide insight into the wake behind an estate vehicle. The results indicate the near wake and base-pressure distribution is dominated by up-wash caused by flow exiting the smooth underbody diffuser.

1. Introduction

Progress in automotive aerodynamic development has been motivated by an increased demand for more energy efficient vehicles, for environmental and economic reasons. For a modern vehicle operating at highway speeds, aerodynamic drag contributes 60% of the overall resistive force (Heft et al., 2012a). In addition, aspects important to a vehicle's operation, such as stability and comfort, are also affected by its aerodynamic shape. There has been an increased consumer uptake of *Sports-Utility Vehicles* (SUVs) in markets such as Australia (Federal Chamber of Automotive Industries, 2017), and continued strong estate vehicle (also termed station-wagons) sales in Europe. Estate vehicles, by significantly increasing the backlight angle for a similar overall length, typically offer increased cargo area and versatile interior configurations. The wake of an estate will differ from an otherwise similar sedan, and as corollary so too will the aerodynamic drag.

The flows behind estates, hatchbacks and SUVs, which all share a similar rear-end configuration, have not been widely studied. The relevant previous studies can be divided into those that have used a simplified model but with a similar back angle and those that use a detailed model (i.e. a production car). These will be considered in turn.

Previously, detailed studies have primarily been focused on generic, simplified geometries, such as the Ahmed (square-back (0°) and 35° slant bodies) (Ahmed et al.), SAE (Cogotti, 1998), ASMO (Aljure et al., 2014), GTS (McArthur et al., 2016; Croll et al., 1996) or Windsor (Littlewood

et al., 2011) models. The wake topologies of simplified models are typically fully separated from the base, and provide a good basis to analyse fundamental, large-scale flow structures, but results are not easily transferable to production cars. Indeed, due to the increased complexity and detail of the geometry of production vehicles, regions of high turbulence and general unsteadiness contribute to the complicated wake structure of such vehicles.

The Windsor and Ahmed models are typically rectangular cylinders with a slanted or rounded front geometry. Various rear slant angles are available for both models. The ASMO model has a square-back rear with a smooth surface, a boat-tail rear and an underbody diffuser. The Ahmed and Windsor square-back models typically have a large lower recirculating vortex driven by underbody flow and a standalone upper vortex formed from the rolling up of flow structures in the separated roof shear layer (Littlewood et al., 2011). For the Ahmed and Windsor geometries, a lateral bi-stability in the wake occurs on a time scale 500 to 1000 times longer than typical von-Karman shedding periods (Grandemange et al., 2013; Perry et al.). This feature is also found to be highly sensitive to small angles of yaw, favouring an asymmetric state (Grandemange et al., 2013; Volpe et al.). However, statistical averaging over a long time period yields a symmetric wake. Grandemange et al. (Grandemange et al., 2015) found an industrial-scale (or passenger vehicle scale) Ahmed square-back to exhibit a bi-stable behaviour after optimising the model's drag through the use of trailing-edge chamfers. The use of a vertical disturbance, or control cylinder was found to suppress the bi-stable

[☆] A realistic, partially de-featured automobile geometry.

^{*} Corresponding author.

^{**} Corresponding author.

E-mail addresses: terence.avadiar@monash.edu (T. Avadiar), david.burton@monash.edu (D. Burton).

behaviour, reducing drag. For the square-back and 35° slant-angle bodies, their recirculation lengths range within 0.33–0.37 of the vehicle length behind the model (Volpe et al.; Lienhart et al., 2002). The ASMO model's time-averaged wake composes of a horseshoe toroidal vortex bounded by the roof and side flow, with slower underbody exit flow forming the recirculation bubble's lower vortex (Aljure et al., 2014). In addition, recent work by Venning et al. (Venning et al.) presented evidence the time-averaged flow structure at the base of an Ahmed body with 25° rear slant angle are a pair of horseshoe vortices whose legs point downstream. With the presence of modern underbody diffusers or body pillars (C or D-pillars) on which longitudinal vortices form, an augmentation to the wake may be present relative to the toroidal ring vortex found for square-back bodies.

Information regarding the time-varying nature of simplified geometries is widely available. The wake of a rectangular body of equal aspect ratio identified two main characteristic frequencies associated with different vortex shedding processes (Duell and George). Duell and George linked these motions with longitudinal pumping of the free-stagnation point and shear-layer vortex shedding, occurring at non-dimensional frequencies (based on height and freestream velocity) of $St_H = 0.069$ and $St = 1.157$ respectively. For the Ahmed square-back, dominant frequencies were found at $St_H = 0.13$ and 0.19 ; a resultant of von Karman-like shedding off the horizontal and vertical edges of the base. In addition, evidence of a near-wake pumping mechanism was also found at a frequency of $St_H = 0.07 - 0.09$. For the 35° slant-angle Ahmed body, a drag-reduction study using active flow control (Brunn et al.) highlighted the target non-dimensional frequencies of $St_H = 0.2$ and $St_H = 0.88$, associated with vortex shedding and shear-layer instabilities, respectively.

The bulk of experimental work on realistic vehicles has focused on the body forces and surface pressures. Drag-reduction efforts have been focused upon examining the effect of common modern passive geometries on the wake, such as roof spoilers (Kremheller, 2014), underbody roughness, rear diffusers (Aronson et al., 2000; Marklund and Lofdahl; Kahlighi et al., 2012), wheel wake control (Aronson et al., 2000; Marklund and Lofdahl), and optimizing the exit location of cooling flows (Kahlighi et al., 2012; Wittmeiere and Kuthada, 2015). These studies indicate the wake of estate-like vehicles with rear diffuser sections are heavily influenced by upwash from the underbody exit flow, convection of the wheel wakes towards the vehicle centreline, and may exhibit a strong lower recirculation region.

A partial solution to address the limitations of testing with highly simplified bodies is to introduce a reference geometry representative of modern production vehicles. The DrivAer model is a detailed generic car model (Heft et al., 2012a). The configurations available for this model include interchangeable tops (fastback, notchback and estate), two underbody geometries (detailed or smooth), wing mirrors, wheels, and recently, a mock power-plant system to simulate cooling and cavity flows (Wittmeiere and Kuthada, 2015).

Preliminary results and studies on the DrivAer geometry highlight differences of the drag coefficient for different vehicle body types. Ahmed's results (Ahmed et al.) show the square-back (0°) or 35° slant angle rear had drag coefficients less than that of the 25° case (commonly studied as a simplified fastback vehicle). Conversely, the initial time-averaged pressure and drag results for the DrivAer model's fastback or notchback configurations are typically 15–20% lower than the estate's drag (Heft et al., 2012a). Such findings indicate the flow topologies of over-simplified geometries are not fully transferable to detailed vehicles, with key flow structures and their interactions being different (Heft et al.; Heft et al.; Wieser et al., 2014).

Geometric features such as wheels and their housings, mirrors, body pillars, and combinations of curved and sharp edges, are examples of such differences that influence external flow and the nature of flow separation. The external flow around the DrivAer body is influenced by the presence of detailed features such as the wheels, wheel-housing cavities, side mirrors, an underbody diffuser and the general vehicle

geometry. Induced and separated flow structures around the DrivAer are of interest to research and industry to understand the losses associated with vehicle operation.

Flow features expected to be similar across the three main DrivAer geometry configurations, with a smooth underbody, will be considered. A-pillar vortices are formed by flow separating off the front windscreen, which is then transported onto the roof (Heft et al.). Remnants of these structures are observed to be present in the wake of the vehicle based on total pressure results (Guilmineau, 2014). Shedding off the wing mirrors also impart losses that are imprinted on the wake of the vehicle (Guilmineau, 2014; Yazdani, 2015), but the effects are of smaller magnitude than the influence from the A-pillar structures. This is possibly due to the collection of boundary layer vorticity of a single sign to feed into the A-pillar vortices on each side, while the wing mirrors have a more localised effect with net cancellation of vorticity of different signs as the fluid advects downstream. Additionally, the presence of the wing mirror is found to diminish the strength of the A-pillar vortices (Heft et al.), with formation no longer commencing at the root of the A-pillar. However, Heft et al. (2012a) note that the increased strength and closer proximity to the rear windscreen has little impact on the rear flow field of the vehicle. Exit flow from the smooth underbody exit of the DrivAer is attached, with large contributions of fluctuations and unsteady flow from the rear wheels being convected toward the center of the vehicle (Heft et al.; Yazdani, 2015) inducing upwash and some unsteadiness (Strangfeld et al., 2013) into recirculation region of the vehicle's wake. This is especially prevalent for the estate vehicle, where a lower vortex system is observed to be more dominant and induces reverse flow onto the rear windscreen of the estate (Yazdani, 2015).

Of interest to this work are studies of estates and similar vehicles (e.g. SUVs and hatchbacks). An experimental and numerical investigation on an SUV by Kahlighi (Kahlighi et al., 2012; Kabanovs et al.; Marklund and Lofdahl; Blacha and Islam) characterized the wake flow in the symmetry plane as a largely symmetric wake, featuring a strong reversed flow region bounded by two shear layers beginning at the top and bottom trailing edges of the model. Experiments and numerical simulations of a detailed SUV showed a strong lower recirculation region and a large degree of upwash. An investigation into soiling on an SUV fitted with a rear underbody diffuser (Kabanovs et al.), showed the strong lower recirculating region that would influence the momentum of entrained flow on the vehicle's backlight. Marklund (Marklund and Lofdahl) conducted a numerical study comparing the performance of an underbody diffuser for a Saab 9-3 sedan and estate (referred to as a wagon) and found the wake of an estate to be dominated by upwash with the presence of an underbody diffuser. The wake of an estate was more symmetric in the vehicle's centreline in comparison to the downwash dominated flow of a sedan. Development of production vehicles such as the Audi Q5 SUV-estate crossover (Blacha and Islam) and Nissan Qashqai SUV (Kremheller, 2014) highlighted the changes to the flow field from geometric features mostly found on estate like vehicles. Time-averaged streamlines on the SUV's back light fitted with a roof spoiler show entrained flow moving up the rear windscreen, which then travels outboard below the spoiler and mixes back into the flow at the body pillar and spoiler interface (Kremheller, 2014). A corresponding increase and recovery in base pressure is observed below the spoiler. Similar pressure distributions exist for a hatchback and transport van, with recovery toward the top of the vehicle fitted with a spoiler (Bonnaivon et al., 2017). Wake asymmetry modes were found for these transport van and hatchback vehicles by Bonnaivon (Bonnaivon et al., 2017), with evidence of both vertical and horizontal switching modes present when the vehicles are aligned with the flow. These modes were especially prominent in yawed conditions, with a substantial impact on the dynamics of the wake.

This paper presents a study of forces, pressures and velocity measurements, and quantities derived from such measurements (e.g. Reynolds stresses, vorticity and turbulence intensity) in the wake of a full-scale DrivAer estate vehicle. By providing a detailed characterisation of

the time averaged (and mean turbulence statistics) flow parameters it is aimed to gain further insight into the main features of estate wake flows especially for the future development of passive and active flow control techniques. Results are also presented for flow features found on the front and side of the vehicle highlighting the complex flow topology that exists on realistic vehicles.

2. Experimental setup

This study was conducted at the Monash Wind Tunnel Platform (MWTP). This facility is a 3/4 open jet closed-loop wind tunnel with a test section measuring $12 \times 4 \times 2.6$ m ($L \times W \times H$). The maximum freestream velocity is 55 ms^{-1} with the freestream turbulence intensity $I_{U_{\infty}} \leq 1.6\%$. A Pitot-static tube is utilised to obtain tunnel wind speed and a reference static and dynamic pressure at the jet exit plane. An additional array of 6 Pitot-static probes are used to calculate wind speed, located upstream of the jet contraction. A dynamic pressure factor is then applied to the spatial average of these probes, providing the calculated air speed at the vehicle's front stagnation point. The secondary Pitot-static tube is used to obtain reference dynamic and static pressure values, assisting with any drag corrections. The change in dynamic pressure at the jet exit plane with and without the vehicle model installed is 1.4%. A ground simulation system was not available.

The DrivAer vehicle measures $4.61 \times 1.82 \times 1.42$ m ($L \times W \times H$), with an aspect ratio, $W/H = 1.28$ and included the estate top, wing mirrors and a smooth underbody. The model comprises of a steel interior frame with a fiberglass skin. Fig. 2 depicts the DrivAer estate model (pictured in Fig. 1) in the MWTP test section. Solid wheels with rubber patches minimized the effects of ride height and attitude variance associated with pneumatic tires. Drag and pressure measurements were conducted with and without side mirrors, employed in the wake velocity measurements.

The blockage ratio for the DrivAer is 20.7% based on the vehicle's frontal area projection (2.16 m^2), and a correction was applied to the drag coefficient estimates using the two pressure gradient approach outlined by Mercker and Cooper (Mercker and Cooper). The Reynolds number, based on length, for the velocity and pressure measurements was 8×10^6 (equivalent to a vehicle travelling at approximately 100 kmh^{-1}). Drag was additionally measured at Reynolds numbers ranging from 6.5 to 11.6×10^6 (found in Fig. 7).

Force measurements were achieved through in-floor 3 component piezoelectric force-transducers at each wheel contact patch for determi-

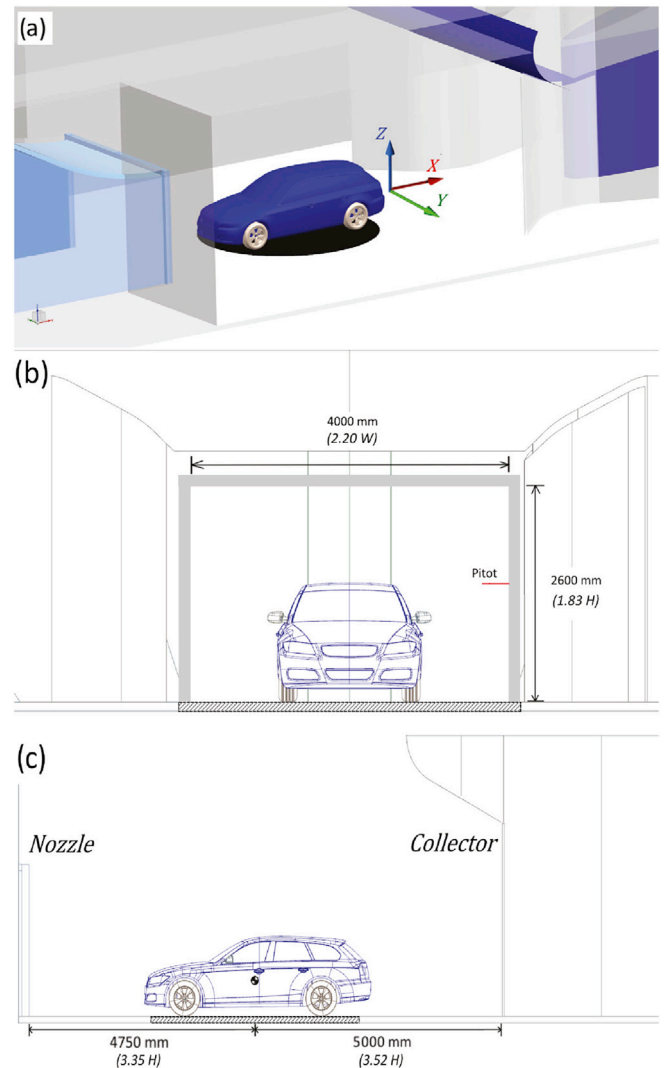


Fig. 2. (a) Isometric CAD representation of the DrivAer model in the MWTP; (b) Front view with nozzle dimensions, with the location of the secondary reference Pitot-static tube indicated; (c) Side View with longitudinal position (from nozzle exit and to collector entrance plane) of the DrivAer. Supplementary dimensions in brackets are given in terms of the model's height and width.

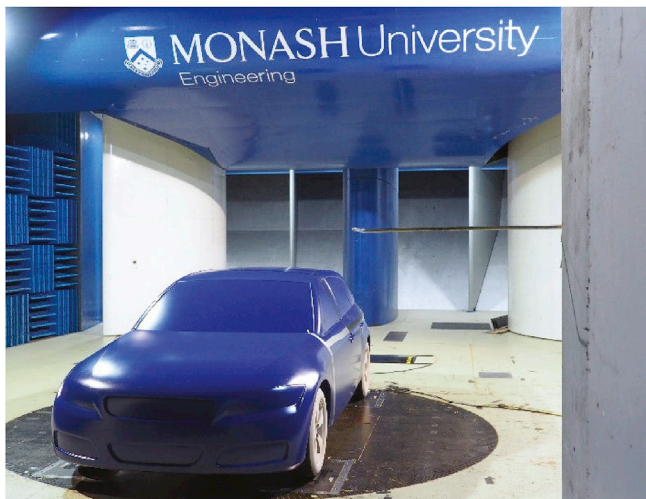


Fig. 1. The DrivAer full-scale vehicle in the Monash Large Wind Tunnel (MWTP) test section. A secondary reference Pitot-static tube is pictured protruding from the side wall. The collector part of the wind tunnel can be seen behind the car.

nation of the 3 principal forces and moments. Force transducer outputs are acquired at 250 Hz and each test sample is averaged over 60 s. Windowed data sets of 15 and 30 s had maximum deviations of 0.5% and 0.07% from the original 60 s duration, confirming a converged value. Repeatability for the drag measurements was found to be approximately $\Delta C_D = \pm 0.0004$. Pressure measurements utilized a synchronous 128 channel *Differential Pressure Measurement System* (Mousley, 2011a) with a tubing length of 1500 mm, allowing for a frequency response of up to 150 Hz. Surface pressure measurements were sampled at 1000 Hz for a duration of 600 s. Tubing corrections for phase and amplitude were applied to the results. A Pitot-static tube (pictured in Fig. 2) at the nozzle exit plane was utilised as a static pressure and secondary upstream velocity reference for base pressure surveys and for wake velocity measurements, relative to the wind tunnel's Pitot-static probes located in the settling chamber. A defined dynamic pressure factor is applied to calculate the velocity in the test section. Dynamic pressures between these sets of probes and at the nozzle exit plane were found to be within 0.5% for both the empty tunnel and with the DrivAer model installed. To account for the longitudinal variation within the test section, the relevant dynamic and static pressure corrections were applied.

Velocity measurements were conducted with two 4-hole dynamic pressure probes, commercially known as the *Cobra probe* (Mousley, 2011b), mounted on an automated mechanical traverse behind the model sampled at 1000 Hz. The probes are able to resolve the three velocity components and output the time-averaged turbulence intensities and the six Reynolds stress components. For such time-averaged velocity magnitudes, flow quantities used for analysis are based upon a minimum of 80% of data failing within the probe's 45° flow incidence calibration range. This approach follows that of recent studies (Bell et al., 2016a; Bell et al., 2016b; Crouch et al., 2014; McArthur et al.), of trains, cyclists and trucks, where probes have been applied to characterize bluff-body wakes. Flow quantities identified as outside this range are rejected by the probe (including reversed flow). To provide further information on the flow, low fidelity results (below the 80% threshold) will be marked by boundaries on contour plots in the results section.

Wake velocity measurements were conducted in the transverse plane on one side of the body at $X/H = 0.5, 1, 1.5$ and 2 . The planes as shown in Fig. 3 measure $1.2H \times 0.8W$ with a uniform grid resolution of 50 mm ($0.035H$). Additional velocity surveys along the model's centreline were conducted at streamwise distances behind the model of $X/H = 0, 0.25, 0.75$ and 0.9 .

The automated mechanical traverse with the mounted probes represents a blockage in the model's wake, the largest obstruction being 2.7% of the jet's cross-sectional area when sampling the 2-D wake velocity planes. For all measurements where the traverse system was utilised, the probe(s) were a minimum of 700 mm ($\approx 0.5H$) away from the front of the traverse. Surface pressure measurements taken at the centerline of estate's base found no change to the shape of the profile. Measurements at $X/H = 0.5$ represent the worst-case, an increase in the coefficient of pressure of 6% matched with a decrease in vehicle drag of 5.2%. The magnitude of changes to the wake closure location, the strength of flow structures presented or Reynolds stresses is expected to be minimal.

In addition to the surveys of the wake, detailed velocity measurements were obtained in the neighbourhood of several key geometry features of the DrivAer estate. Lateral velocity sweeps were done at $Z/H = 0.3$ and 0.5 , focused on the side shear layers. These locations correspond to certain geometry features, the rear bumper and tail-lights, respectively. Roof shear layers were also measured at 3 longitudinal positions rearward of the roof spoiler's edge ($X/H = 0, 0.05$ and 0.15).

Flow visualisation was employed to elucidate the flow structures influence on the vehicle's surface and their behaviour in the wake. Surface flow-visualisation using paint or ink droplets aim to show the skin friction velocity lines on the model's surface, providing information on the influence of flow structures acting on the surface. The paint flow mixture comprised of kaolin, fluorescent pigment and a kerosene carrier. Exper-

iments were conducted at a Reynolds number, based on body length, of 8.5×10^6 with a ramp up time of 30 s from application, with the paint or ink droplets allowed to set (once streaks were beginning to dry) at a steady wind condition for a minimum of 2 min. This period of time was set to ensure gravity did not materially affect results as the tunnel was subsequently ramped down.

2.1. Ground boundary layer

A limitation of this experiment is the fixed-floor of the wind tunnel; for this reason the boundary layer (BL) was measured at several locations along the test section centreline. For the purposes of measuring the bulk rear wake of the DrivAer, the largest concern lies with the height and growth of the BL. The height of the ground boundary layer was determined using a 4-hole dynamic pressure probe at different locations along the empty tunnel floor. Measurement locations included the positions of the DrivAer's nose, center and tail.

Fig. 4 shows the empty wind tunnel BL height of $Z = 0.12H$ at the nose and $0.13H$ at the centre of the vehicle, larger than the minimum ground clearance of $0.10H$. The displacement thickness, δ^* at both these locations was approximately 14% of the ground clearance. The authors acknowledge that the influence of an increased ground BL may unrealistically increase the underbody exit flow velocity, due to the decreased effective ground clearance if considering the physical interpretation of the displacement thickness. However, whilst the strength of the flow structures may be changed from augmented flow regimes around the wheels and below the rear diffuser, the flow topology is expected to remain largely unchanged. Implications of the ground BL on the wake topology will be discussed where relevant in the results section of this paper. The impact of the vehicle's presence on the localised ground BL due to large local pressure gradients and changed flow conditions on the baseline empty-tunnel BL properties will also be discussed.

In order to ascertain the influence of the ground boundary layer, centerline base pressure results (provided courtesy of Ford Motor Company) on the same full-scale DrivAer model used in this study was obtained at Tongji's full-scale automotive wind tunnel. Three different studies are shown in Fig. 5, the MWTP results, Tongji with ground simulation active, and Tongji with ground simulation off. For the inactive ground simulation study at Tongji, upstream boundary layer suction was active. The ground BL thickness for the fixed ground study at Tongji is estimated to be approximately 34% of the MWTP's ground BL at the centre of the vehicle's wheelbase (Xia et al., 2016). The centerline pressure distribution across the different facilities follow a similar trend with the pressure recovery on the underbody, especially important in evaluating properties of the DrivAer's wake with the presence of a rear diffuser.

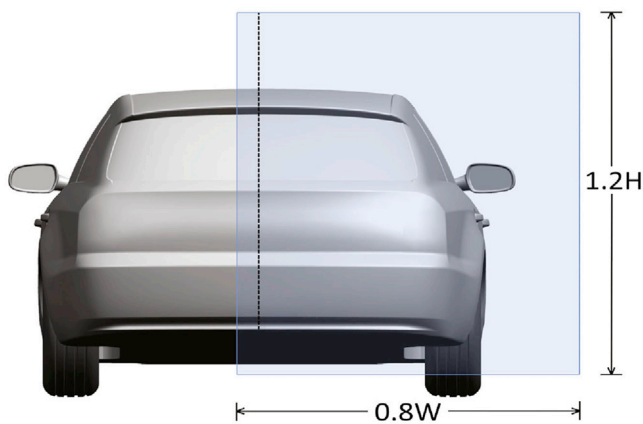


Fig. 3. YZ Plane bounds for transverse plane wake velocity measurements with a spatial resolution of 50 mm ($0.035H$), taken at $X/H = 0.5, 1, 1.5$ and 2 . The dashed line represents the vehicle's centerline.

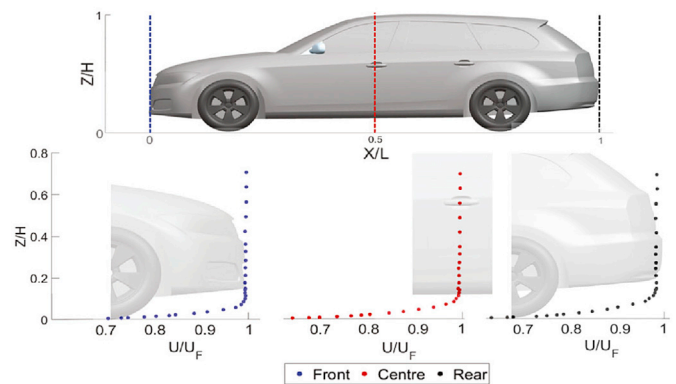


Fig. 4. Empty wind tunnel ground boundary layers measured at longitudinal positions corresponding to front, centre and rear of the DrivAer estate (vehicle insets are included on each plot for reference of the model's position relative to the empty WT results).

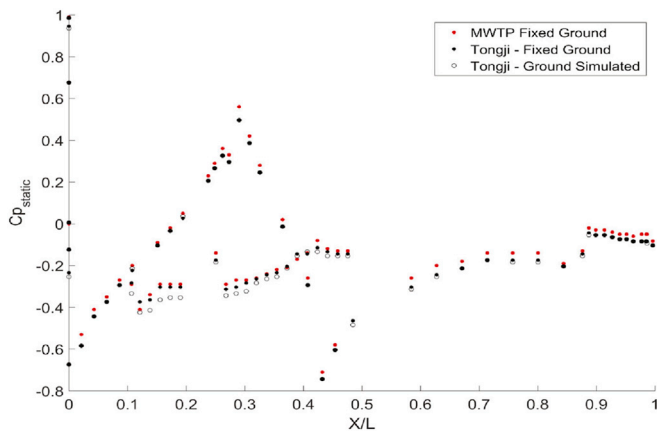


Fig. 5. Centerline base pressures over the top surface and smooth underbody for the full-scale DrivAer model tested at two wind tunnel facilities. Three configurations presented are fixed ground at MWTP, and both fixed ground and simulated moving ground conditions at the Tongji facility.

2.2. Static pressure gradient

Longitudinal static pressure profiles at two different heights (estimated stagnation point height, $Z = 0.4\text{ m}$ ($Z/H = 0.28$) and 1 m ($Z/H = 0.7$)) were obtained for the different collector configurations of the wind tunnel setup (see Fig. 6). This was done to ascertain if significant effects of horizontal buoyancy may be present for a vehicle being tested. With the estate having a large bluff-body wake, the observed uniform rise in static pressure at the two different heights is expected to have an equal effect on the top and bottom large-scale mean flow structures. A different static pressure profile between the two measurement heights would have possible implications on the augmentation of the near wake, but Fig. 5 shows similar pressure distributions at the rear of the vehicle between tests conducted at two different facilities.

3. Results

Presented below are the results of body force, base pressure, wake velocity measurements and flow visualisations. Unless otherwise stated, these measurements were collected at a Re_{Length} of 8×10^6 .

3.1. Body forces and Reynolds number influence

The drag coefficient for the baseline estate vehicle are provided in Table 1, within 5% of the measurements by Heft et al. (2012a), Ashton (Ashton and Revell, 2015) and Collins et al. (Collin et al.). The measured drag coefficients (C_D) are in good agreement, within 2% of Heft et al.'s fixed ground results, and the drag contribution of the wing mirrors ($\Delta C_D = 0.014$) was found to match that of Heft et al. (2012a).

The sensitivity of drag coefficient within a range of realistic opera-

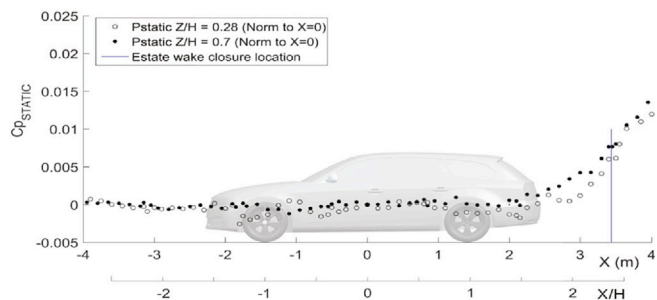


Fig. 6. Centerline empty tunnel distribution at the heights of 0.4 m ($Z/H = 0.28$ - front stagnation point height), and 1 m ($Z/H = 0.7$).

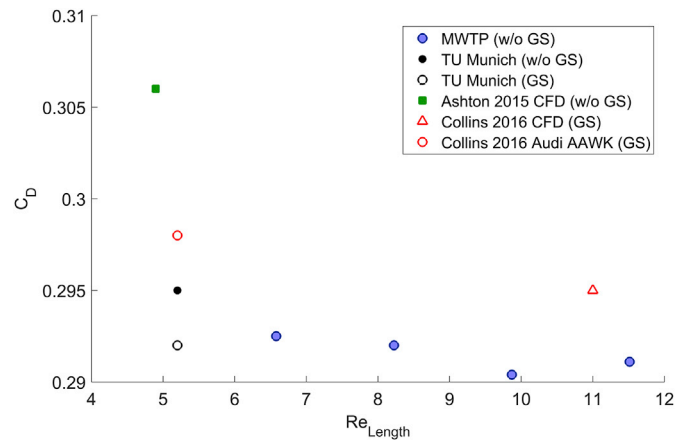


Fig. 7. Progression of measured drag coefficients with Reynolds number. Results include currently available literature results for non-ground simulation studies, as marked in the legend.

Table 1

Drag coefficients for the DrivAer estate vehicle in the ES_wM_wW. Reynolds numbers (based on length) in millions (M) and ground simulation method (Ground Simulated - GS or Fixed Ground - FG) is provided. WT refers to wind tunnel experiments and CFD to numerical predictions.

Study:	C_D	Re (M)	GS/FG
WT (MWTP)	0.291	8	FG
WT (TUM (Heft et al., 2012a))	0.296	5.2	FG
WT (TUM (Heft et al., 2012a))	0.292	5.2	GS
CFD (IDDES (Ashton and Revell, 2015))	0.306–0.313	4.9	FG
CFD (DDES (Collin et al.))	0.295	11	GS
WT (AAWK (Collin et al.))	0.298	5.2	GS

tional Reynolds numbers ($60 - 140\text{ km/h}$) as shown in Fig. 7 was found to be small, changing by less than 0.5% over the range of $Re_{Length} = 6.5$ to $11.6 (\times 10^6)$. There was little expected dependency on drag from the increase in Reynolds number owing to the fully separated nature of the near wake, changes largely attributed to the variation in boundary layer development. In addition, Heft et al. (2012a) concluded that the estate geometry is not influenced significantly by ground simulation in the cases of closed wheelhouses and with wheels, explaining the similarities observed.

3.2. Base pressure distribution and mean statistics

The mean base pressure distribution for the DrivAer estate vehicle is shown in Fig. 8. Base pressures were normalised by the stagnation pressure at the front of the vehicle and the local corrected static pressure, shown by Equation (1) below. The correction for local static pressure was referenced to the turntable center (middle of wheelbase) from an upstream Pitot-static tube at the jet exit.

$$C_p = \frac{P_{sampled} - P_{static}}{P_{stagnation,front}} \quad (1)$$

A large low pressure region is present at the rear tailgate (approximately $Y/W = \pm 0.2$, $Z/H = 0.4$), likely to be influenced by a lower recirculating vortex. This region extends along the line of the rear bumper and moves up diagonally towards a minimum at the tail lights ($Z/H = 0.6$). The low pressure distribution indicates the time-averaged wake's outboard section of the lower recirculation region approaches closer to the body. In addition, recovery towards the vehicle's centerline suggests the influence from a vortex system is reduced. The base pressure gradually increases vertically on the upper half of the windscreen and is quite uniform across its width.

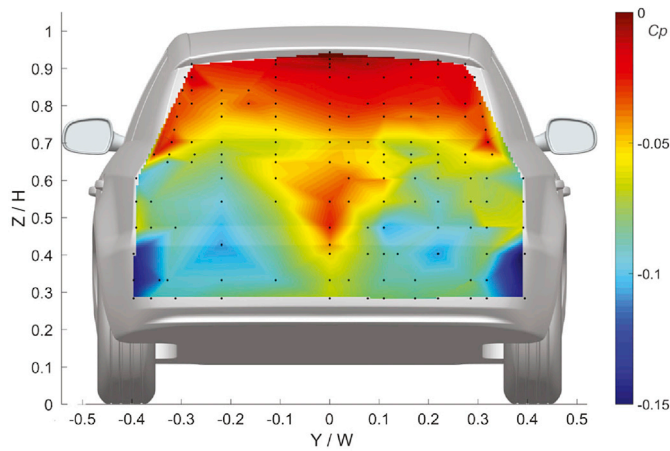


Fig. 8. Mean base pressure distribution.

On the underside surface of the spoiler, pressure values approach ambient conditions, indicating this may be a region of flow close to stagnation. These findings are consistent with initial rear windscreen pressure results by Heft (Heft et al., 2012a) and base pressure contours from numerical simulations by Yazdani (2015). Moreover, the presence of a low pressure region at the bottom, with recovery toward the top of the model has been similarly observed on the Windsor body (Littlewood et al., 2011), and realistic square-back vehicles (Bonnaïon et al., 2017).

The proposed outboard movement of flow at the top of the rear windscreen will likely disturb the formation of the D-pillar vortices, as Fourrie et al. (2011) found for a spoiler on a 25° slant Ahmed body. In addition, the shear layer vortices off the roof are expected to interact with the negative vorticity from flow travelling up the rear windscreen similar to Fletcher and Barbuto (1986) findings for a short-lipped backward-facing cavity. In view of potential drag reduction efforts, the ratio of spoiler length and angle may indeed be of interest, balancing the expansion of the roof shear layer and the formation and subsequent emission of any secondary eddy cells that may form below the spoiler's surface (Fletcher and Barbuto, 1986).

An area integral projected in the x direction, using a trapezoidal approximation of the base pressure drag results in (C_D) pressure drag = -0.147 or 51% of the total drag. This base drag contribution is approximately 73% of the DrivAer estate vehicle body only level (wheels and wing mirrors omitted), based on the values previously published in Heft et al. (2012a).

The standard deviation of base pressures in Fig. 9 depict regions of high fluctuations at the curved trailing edge surfaces on the base of the vehicle, potentially due to a non-fixed separation location of flow over a

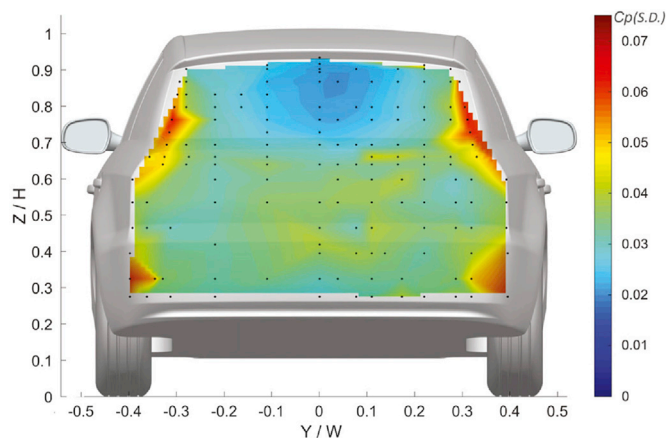


Fig. 9. Distribution of the standard deviation of base pressure.

curved surface on the bumper or D-pillars. Of interest, this region does not correspond to the highest magnitude negative pressure.

The pressure recovery region below the spoiler in Fig. 8 may be considered to be a largely steady region that experiences larger fluctuations progressing outboard toward the D-pillars. Local low pressure regions at approximately $Y/W = \pm 0.2, Z/H = 0.4$ proposed to be a region of influence from a lower recirculating vortex system is observed to have a relatively moderate degree of fluctuations.

Three pressure measurement points in regions of high and low fluctuations in pressures (large and small standard deviation) are examined closely in Fig. 10. Of interest is the comparison between the D-pillars taps ($Z/H = 0.78$) which exhibits relatively high mean base pressure, yet has a high degree of fluctuation and a negatively skewed probability

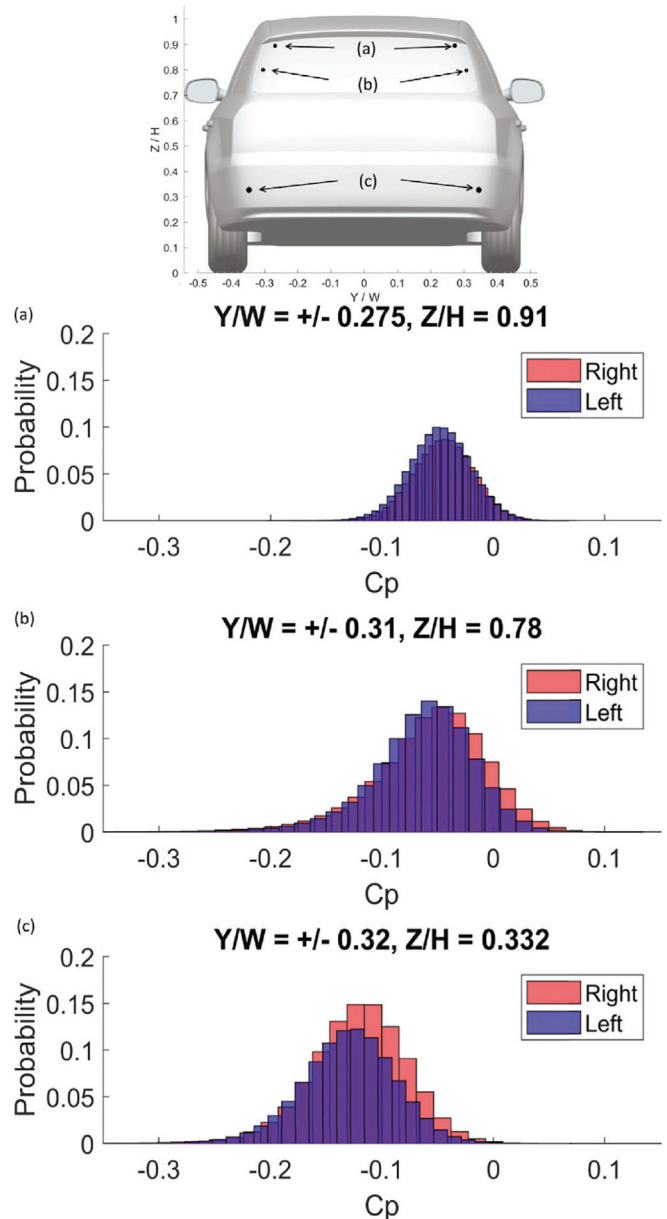


Fig. 10. Probability distribution of the pressures located at various locations corresponding to regions of low standard deviation and high standard deviation. From top to bottom, the location of the taps investigated, (a) the probability distribution of the outboard edge directly below the spoiler, (b) the outboard edge at the D-pillar and (c) the bumper location where the local radius is approaching the minimum change in curvature.

distribution, suggesting an interaction with the shear layer at this point. At the higher tap ($Z/H = 0.91$) a similar mean pressure is observed, however the lower standard deviation indicates that this is a relatively quiescent region.

At $Z/H = 0.332$, near the corner of the rear bumper, the mean negative base pressure magnitude is highest, and high level of fluctuation is observed. It is unclear whether the turbulence from the upstream rear wheel wake contributes significantly to the unsteadiness observed at the bumper, or if turbulence influences the separation location (Buresti et al., 1997). Future work to ascertain if the spectra of the time-varying signal from these rear bumper pressure taps bear similarities to that of the velocity wake data whose averaged results are presented later on in this paper.

3.2.1. Flow bi-stability

The estate vehicle is of the type that may exhibit a bi-stable or the more global symmetry breaking modes, as has been identified for other vehicle-type bodies by Grandemange (Grandemange et al., 2013; Volpe et al.), and more complex symmetry breaking modes recently by Bonnavion (Bonnnavion et al., 2017) for hatchback vehicles. An attempt was made to identify such a feature by subtracting the respective left and right pressure taps at various locations along the body (i.e. taps located equidistant from the centreline of the vehicle) see Fig. 11 (top). A first-order low-pass Butterworth filter at 10 Hz was applied with the amplitude damping starting past the frequency corresponding to a Strouhal number of 0.5. The probability distribution (P.D.) of these pressure differences is shown in Fig. 11 (middle) and no clear bi-modal features are apparent, except at $Y/W = \pm 0.391$, although this is certainly not clear.

To further investigate the existence of any bi-stability bias (should any exist), the sign of the horizontal pressure gradient across the rear surface was determined. A least-squares linear line of best fit was used across 9 pressure taps at $Z/H = 0.54$ for the horizontal gradient, shown in Fig. 11 (top), the same calculation was also performed using 2 pressure taps. The wake is assumed to be in either a left or right state according to Equation (2) below.

The gradients between the pressure taps shows periods of favouring one side relative to the other. However, the wake also displays extended periods where the gradient oscillates from positive to negative, such that from these results a bi-stability in the wake has not been clearly identified. The mean time-scales for switching are largely within an order of magnitude of typical von-Karman switching ($\approx 67\%$), although time-scales an order of magnitude higher do exist but are very infrequent, shown in Fig. 12. These higher time scales would include oscillations associated with vortex-structure emission from the recirculation region (Duell and George; Bonnnavion et al., 2017), noting a time scale that is typically a multiple of 3–4 times longer than the von-Karman shedding period. Bonnnavion et al. (2017) noted that symmetry-breaking modes were clearly present at yaw, but not prominent for a vehicle symmetrically aligned with the flow. Hence, for this vehicle a bi-stability may also exist at yaw.

The existence of a top-bottom, or vertical, bi-stability, similar to that found by Bonnnavion et al. (2017) for a vehicle at yaw (Bonnnavion et al., 2017) was investigated as part of a larger multi-stability analysis. Fig. 13 shows a histogram and time trace of a least-squares linear fit for the centerline taps. Over the entire time domain, the gradient remains positive, indicating the lower half of the estate experiences the largest magnitude pressures (according to Equation (3)), suggesting the lower vortex is indeed dominant. The top two taps, corresponding to the underside of the spoiler and upper edge of the rear windscreen, were excluded from the data set to minimise the influence of any local flow phenomena (such as stagnation or small flow structures below the spoiler). The standard deviation for the data inclusive of the rear windscreen topmost taps were correspondingly found to be 6% lower, confirming that a “damping” of the gradient existed, although the trends prove identical over the entire time-domain.

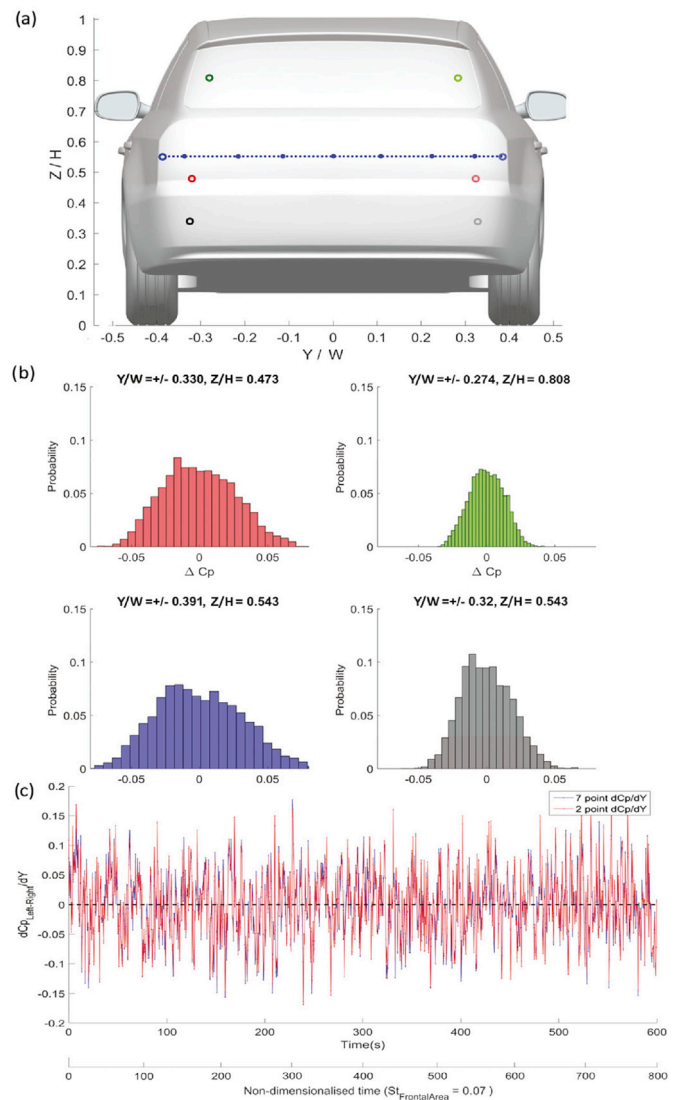


Fig. 11. The locations (a) of the respective left and right pair of pressure taps to determine the existence of bi-stability. Histograms (b) show the P.D. of the detrended left-right pressure signal at certain locations. The least squares linear fit for the set taps at $Z/H = 0.54$ versus time (c), plotted with a rolling 2 s average applied.

$$\text{Left state : } \frac{dC_p}{dY} \geq 0; \text{ Right state : } \frac{dC_p}{dY} \leq 0. \tag{2}$$

$$\text{Bottom state : } \frac{dC_p}{dZ} \geq 0; \text{ Top state : } \frac{dC_p}{dZ} \leq 0. \tag{3}$$

Periods of large changes were found in the gradient, approximately an order of magnitude longer than an estimated low frequency pumping of the wake (Duell and George; Volpe et al.) of $\approx St_{FrontalArea} = 0.07$. The cause for these periods remains to be fully fledged, and if the states are related to global detachment of the large-scale structures from the base or reattachment of flow onto the rear windscreen as found by Bonnnavion (Bonnnavion et al., 2017). However, the probability distribution appears to be close to that of a normal type, with no clear secondary peaks present to suggest a clear bistable mode is dominant. For the case with the top two pressure taps excluded, 5.5% of the data was outside the 95% confidence interval for the linear gradient's mean, suggesting mode events may occur.

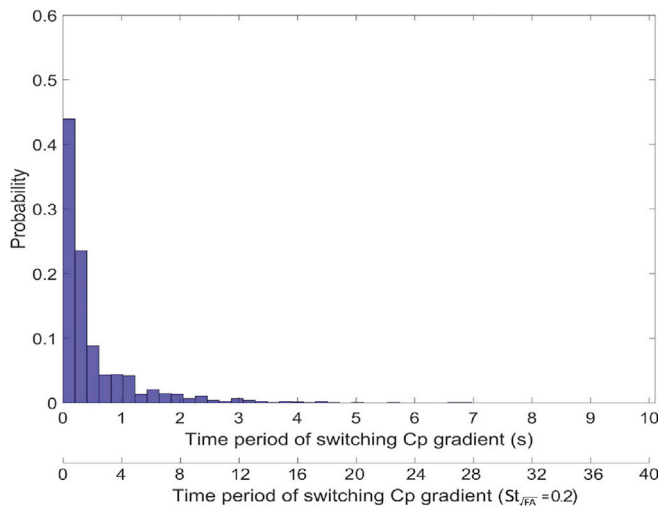


Fig. 12. Probability of timescales for the gradient of the 7-point least-squares fit across pressure taps at $Z/H = 0.54$ to switch signs (ie favour a left from right state and vice versa). The time period (given in seconds and a typical von-Karman shedding frequency) is calculated by interrogating if a sign switch occurs in the gradient, and determines the elapsed time since the prior sign switch event.

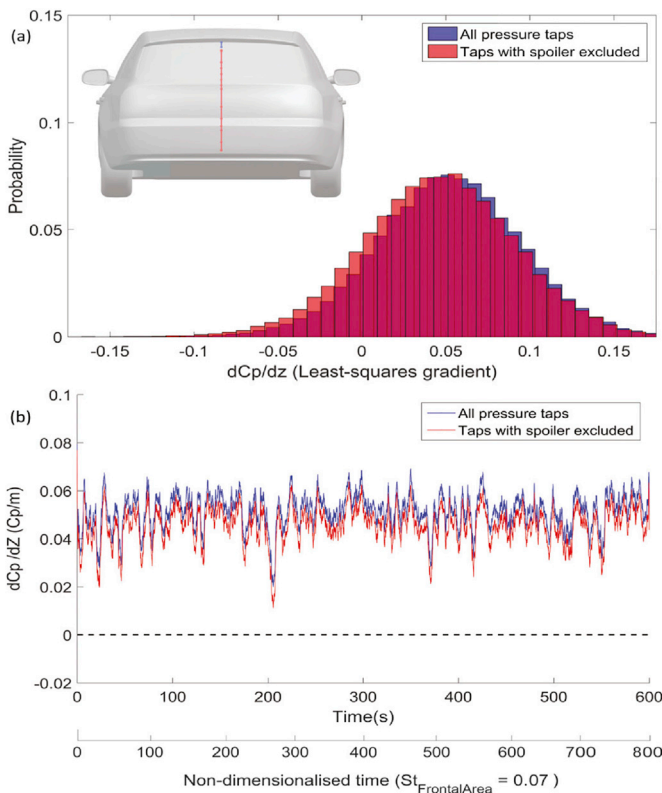


Fig. 13. (a) Histogram of a least-squares linear fit's gradient applied to centerline base pressure taps. The locations (inset) of the pressure taps shown are used to determine the existence of top-bottom bi-stability with and without the top two pressure taps (in blue) on the rear windscreen. (b) The least squares linear gradient for the set taps at $Y/W = 0$ versus time, plotting the result including all pressure taps and a fit excluding the top rear windscreen taps. A positive gradient indicates a low pressure dominates on the lower half of the estate's base. (For interpretation of the references to colour in this figure legend, the reader is referred to the Web version of this article.)

Initial analysis presented here of the left-right and top-bottom favouring periods and evidence of modes is limited, but the respective dynamics of these results as part of the estate's wake as whole are intended to be examined in the future.

3.3. Wake velocity measurements

The following sub-sections depict the wake of the estate vehicle dominated by the upwash from the underbody exit flow, with strong lateral inboard flow at the vehicle's sides. A resultant time-averaged longitudinal vortex dominated by upwash at the centreline of the vehicle is present, likely linked to the proposed lower vortex system based on the base pressure results. Flow exiting the underbody is found to be steady, and the boundary layers at the top and bottom of the vehicle are considerably thinner than the sides, owing to the accelerated flow present.

The streamwise turbulent energy confirms a wake closure height of approximately $Z/H = 0.65$ to 0.7 , corresponding to regions of increased fluctuations that would be expected with the nature of a free stagnation point and pumping of the near wake. The wheel wake of the DrivAer is observed to be convected inboard towards the vehicle centerline but not vertically up, confirmed by the streamwise vorticity contours from $Z/H = 0.5$ to $Z/H = 1$.

The normal and shear components of the Reynolds stresses elucidate the nature of such turbulent fluctuations observed. Observations specific to the DrivAer geometry's shear layers includes non-uniform shedding along the spoiler's edge, negative shear close to the centreline of the vehicle related to the strong upwash that influences the lateral flow moving inboard and significant unsteadiness for the top and side shear layers dominant progressing downstream. It is unlikely that the underbody exit flow is a large contributor to fluctuations, with the largest contributions to vortex emission coming from the spoiler, side edges and free stagnation point.

3.4. Shear layer measurements

The horizontal shear layer profiles measured at two heights ($Z/H = 0.3$ and 0.5) corresponding to the bumper and tail-lights are presented in Fig. 14, respectively. At the rear bumper ($Z/H = 0.3$), there is a greater streamwise velocity deficit and increased turbulence intensity, relative to $Z/H = 0.5$, likely related to the influence of the upstream wheels and cavities. In addition, the lateral velocity at the bumper is towards the centre of the vehicle. The vertical component (w/U_F) is pitched down inboard of the widest point of the rear bumper, possibly caused by induced downwash acting on the bumper's surface, resulting from the influence of a lower recirculating vortex in the wake. The defined separation point at the rear tail-lights ($Z/H = 0.5$) causes a sharp decrease in the lateral velocity inboard of the separation point.

At both heights, the streamwise turbulence intensity follows two different regimes, apparent as a change in gradient, being almost linear when the probe moves inboard of $Y/W = 0.4$. This change in gradient aligns with the approximate separation point of the flow for the tail lights and the beginning of the bumper's curvature. The contribution of the wheel wake to the magnitude of fluctuations on the bumper's shear layer is not fully quantifiable, but comparison of the streamwise turbulence intensity between the two heights reveals an increased magnitude until $Y/W = 0.6$ with a 10% larger degree of fluctuations in the shear layer approaching the bumper's outboard edge. Findings by Marklund (Marklund and Lofdahl) and Aljure (Aljure et al., 2014) found estate-like vehicles would convect the wheel wake inwards, in comparison to a sedan (Marklund and Lofdahl).

Flow off the roof spoiler, Fig. 15, shows a similar trend in streamwise velocity at the three longitudinal distances ($X/H = 0, 0.05$ and 0.15) with a slight increase in velocity in the shear layer at increasing downstream distance. The vertical velocity plot (w/U_F) in Fig. 16 shows a sharp pitched down flow at the trailing edge, an expected result for flows

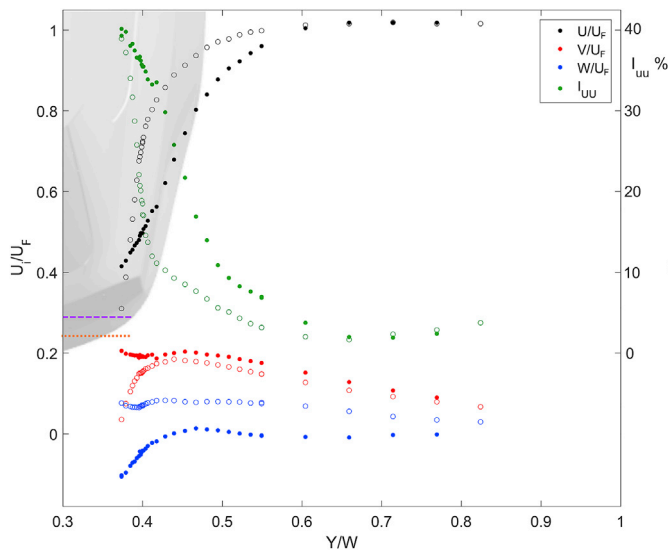


Fig. 14. Shear-layer velocity measurements at the rear bumper ($X/H = -0.05H$, $Z/H = 0.3$ – solid markers) and rear tail lights ($X/H = -0.07H$, $Z/H = 0.5$ – hollow markers). The left vertical axis indicates the respective velocity ratios and the turbulence intensity (normalised by local mean velocity) on the right axis. The purple dashed and orange dotted lines indicate the measurement line location relative to the vehicle for the bumper and tail lights. (For interpretation of the references to colour in this figure legend, the reader is referred to the Web version of this article.)

over a sharp trailing edge (Collin et al.). Progressing downstream, the peak vertical velocity magnitude decreases. Turbulence intensity plotted in Fig. 17 show a relatively linear region over $0.04H$ (extending vertically from just below the roof spoiler radius) with a consistent gradient over the three different longitudinal positions. The top shear layer therefore remains similar over this distance downstream. The sharp rise in turbulence intensity is expected below the surface of the spoiler as the near wake flow is convected back into the shear layer.

Estimates of the boundary layer height, displacement and momentum thickness can be found in Table 2 using measurements from the roof and side (rear tail-lights) of the estate vehicle. Results show the boundary layer to be thinner on the roof than on the vehicle's side. The calculated

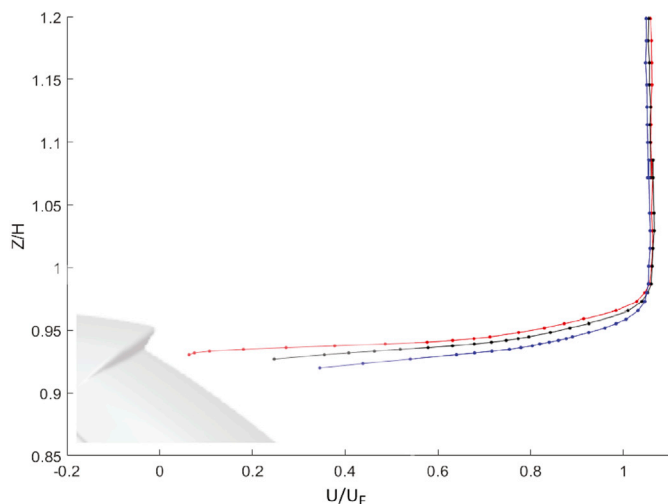


Fig. 15. Streamwise velocity (U/U_F) measurements at three longitudinal distances behind the spoiler's trailing edge ($Y/W = 0$, $X/H = 0, 0.05, 0.15$ correspond to red, black and blue lines respectively). (For interpretation of the references to colour in this figure legend, the reader is referred to the Web version of this article.)

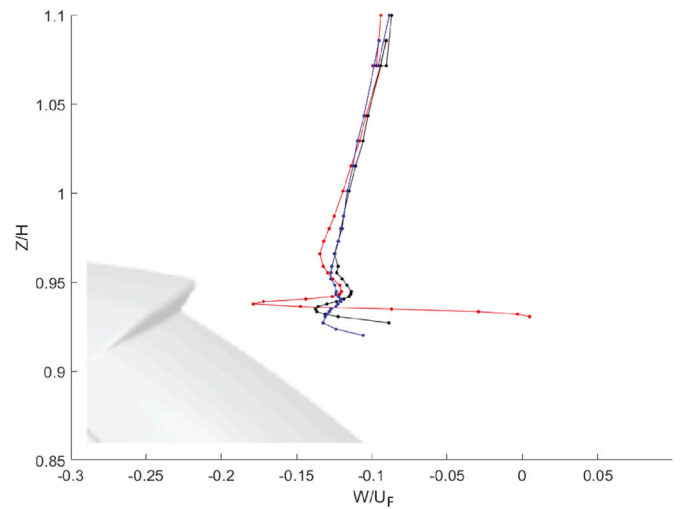


Fig. 16. Vertical velocity (W/U_F) measurements at three longitudinal distances behind the spoiler TE ($Y/W = 0$, $X/H = 0, 0.05, 0.15$ correspond to red, black and blue lines respectively). (For interpretation of the references to colour in this figure legend, the reader is referred to the Web version of this article.)

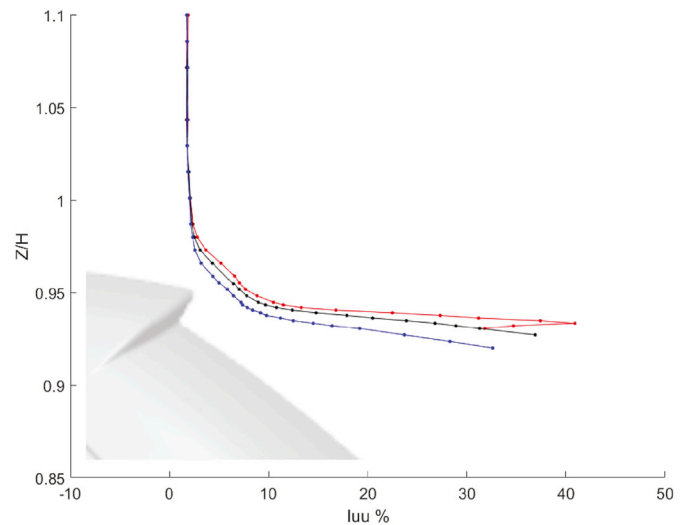


Fig. 17. Streamwise turbulence intensity (I_{UU}) measurements at three longitudinal distances behind the spoiler TE ($Y/W = 0$, $X/H = 0, 0.05, 0.15$ correspond to red, black and blue lines respectively). (For interpretation of the references to colour in this figure legend, the reader is referred to the Web version of this article.)

Blasius solution using a development length of 4.4 m or $X/L = 0.95$ is approximately 68 mm thick. Given the accelerated, and generally attached flow over the bonnet and windscreen, it is not surprising to see the thin boundary layer that is present at the trailing edge of the roof. Boundary layers measured at the side (at the two different heights corresponding to the rear bumper $Z/H = 0.3$ and tail-lights $Z/H = 0.5$) are both observed to be similar in thickness and substantially thicker than the roof boundary layer.

3.4.1. Centerline wake velocity plane (X-Z)

The centerline velocity results presented here are a combination of measurements from the transverse $Y-Z$ plane results and additional centerline velocity surveys conducted, all measured using a 4-hole dynamic pressure probe. Streamwise velocity (U/U_F) profiles along the symmetry plane, presented in Fig. 18, allow for several observations regarding the characteristics of the wake.

Table 2

Inferred BL measurements (given in mm) detailing the BL height, displacement thickness, momentum thickness and the dimensionless shape factor from roof and side shear layer measurements. Bumper BL measurements additionally utilises the change in turbulence intensity gradients from Fig. 14 to estimate the boundary layer height of the bumper, hence denoted by the asterisk.

Location	U_{99}	δ^*	θ^*	H
Spoiler TE (Top BL)	52	7.4	3.2	2.31
Tail lights (Side BL)	245	32.8	24.0	1.36
Bumper (Side BL*)	250	55.5	37.9	1.46

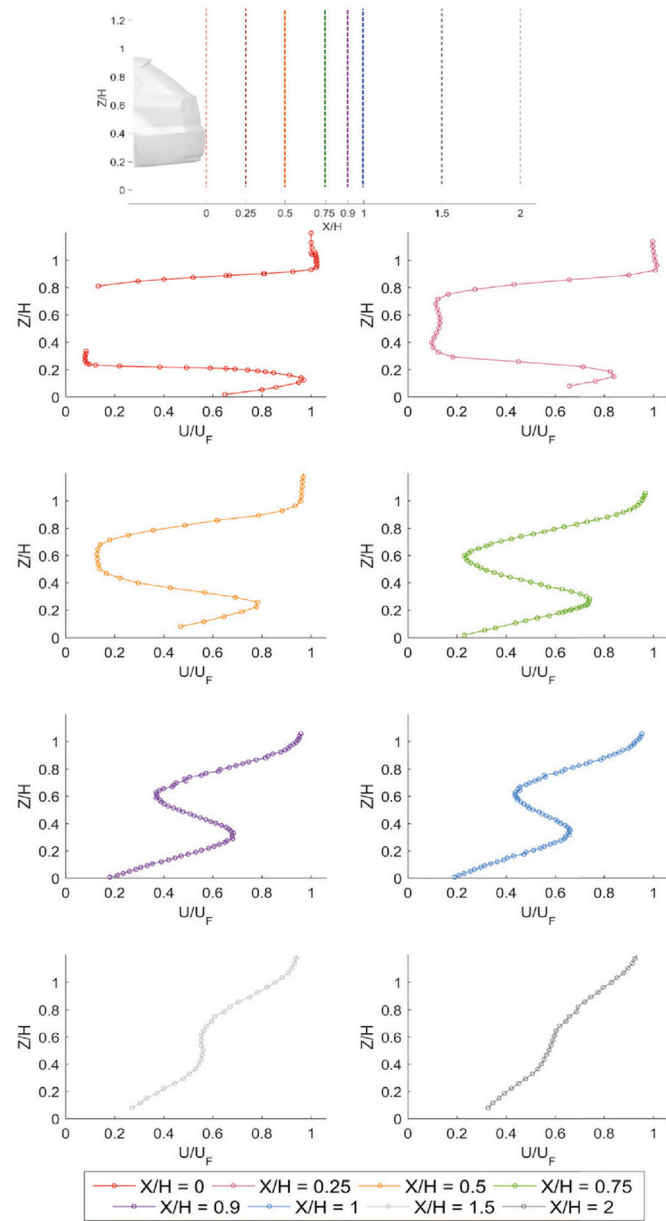


Fig. 18. Normalised streamwise velocity profiles along the symmetry plane at (from top to bottom, left to right) $X/H = 0, 0.25, 0.5, 0.75, 0.9, 1, 1.5$ and 2 behind the vehicle. Top image shows the locations at the rear of the vehicle.

High velocity underbody exit flow is present up to $X/H = 1$ from the rear of the vehicle, consistent with findings from numerical studies completed previously (Wang et al., 2016), with peak underbody exit flow ($U/U_F = 0.84$ at $X/H = 0.25$) comparing well to results from Collins et al. (Collin et al.; Vino et al., 2005) ($U/U_F = 0.88$) and Ashton et al. (Ashton and Revell, 2015) ($U/U_F = 0.83$). This region of accelerated

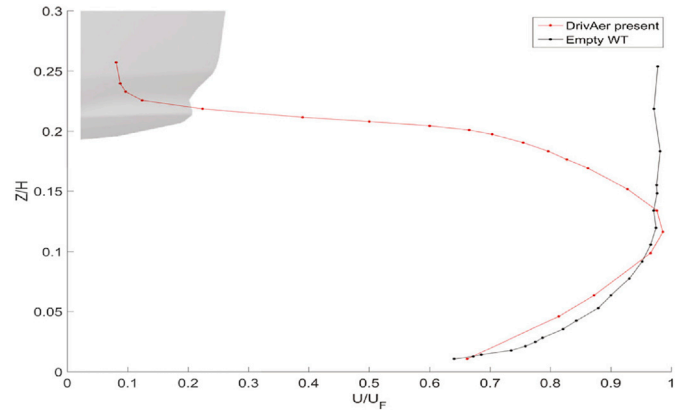


Fig. 19. Comparison of the streamwise velocity component (U/U_F) close to the ground at $X/H = 0$ (vehicle's rear), between empty tunnel BL measurements and with the DrivAer present.

underbody flow is dominant until $X/H = 1$, diminishing greatly at $X/H = 1.5$ and 2 .

Fig. 19 highlights the difference in streamwise velocity at the trailing edge of the vehicle, the ground BL height at the trailing edge of the vehicle to be $\approx 80\%$ of the empty WT configuration. The ground BL profile has also slightly changed, a more linear rise from $Z/H = 0.05$, rather than the fully-developed profile in the empty WT. Flow displacement due to the BL growth may locally accelerate the underbody flow, however this is likely offset by the higher friction associated with the stationary floor (compared to moving ground case) and a lower underbody mass flow caused by displacement effects from the upstream boundary layer. Reduced resolution in the data with a vehicle present near the ground ($Z/H \leq 0.05$) may influence the BL profile shape presented, if considering the impact increased turbulence would present closer to the surface. However, the height location corresponding to the maximum U/U_F or profile shape of the underbody exit flow "jet" will likely remain largely unchanged.

Further downstream, the location of maximum streamwise underbody exit velocity increases vertically, indicating the presence of strong upwash. Streamwise velocity results indicate underbody exit bulk flow is attached. Flow leaving the trailing edge of the underbody was found (Fig. 20) to have a pitch of 14.8° , corresponding to the largest mean upwash flow at this downstream location, and aligning with the underbody's trailing edge of 15° rake angle (Detail A, Fig. 20). The location of maximum pitch (upwash) is located higher than the position of

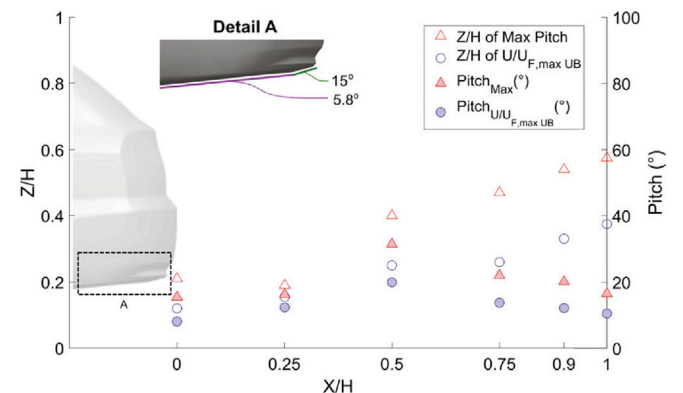


Fig. 20. Vertical locations of maximum pitch and their corresponding values for regions of upwash from underbody outflow only. Local pitch angles for maximum underbody-source streamwise velocity (U/U_F) and respective heights of maximum streamwise velocity are also plotted. Detail A shows the smooth raked underbody gradients, a reference for interpreting the outflow pitch angles.

maximum U/U_F at $X/H = 0$ and 0.25. Conversely, the height corresponding to maximum U/U_F in Fig. 20, increases over $X/H = 0$ to 0.5, the upwash pitch angle also increasing in magnitude.

As the streamwise velocity becomes near symmetric about the half height of the vehicle, approximately from $X/H = 0.75$ to 1, it is proposed the time-averaged near wake is fully closed by approximately $X/H = 0.75$. This compares well with the numerical results by Collins et al. (Collin et al.), with an estimated wake closure point at $X/H = 0.8$. The vertical location of the free stagnation point is estimated at $Z/H = 0.62$, based upon the subsequent deficits in streamwise velocity data and change in velocity measurements inside the acceptance cone of the probe, indicating a reduction in the level of flow reversal. Streamwise and vertical velocity contours in Figs. 21 and 22 show strong upwash present in the vehicle wake at $X/H = 0.5$.

Downwash from the roof of the vehicle remains present in the near wake of the vehicle. Across the length from $X/H = 0$ to $X/H = 0.5$ ($0.06H$ at spoiler TE) the roof shear layers grow in vertical dimension from approximately $0.14H$ to $0.26H$. It is likely that the thin boundary layer over the roof is expected to see the formation of Kelvin-Helmholtz instability waves. The streamwise turbulence intensity is provided in Fig. 23, which shows a large band of fluctuations coming off the roof being convected downwards. The underbody exit flow is confirmed to be steady and attached prior to separation. A local peak in turbulence intensity ($X/H = 0.9$) is consistent with the proposal of a free stagnation point indicating the wake closure at $Z/H = 0.62$.

3.5. Transverse wake velocity planes (Y-Z)

Velocity profiles taken in the Y-Z plane in the wake of the vehicle are presented in Fig. 24. These show the progression and development of structures over the distance $X/H = 0.5$ to 2.0. At the minimum distance from the vehicle tail ($X/H = 0.5$) the flow toward the vehicle centreline has a large degree of upwash and inward lateral flow around the mid height at the vehicle sides. Whilst some downwash is observed towards the vehicle roof, by $X/H = 1.0$ the downwash between $Y/W = 0$ and 0.2 has weakened and flow is nearly entirely upwards. The lateral inwards flow together with the upwash creates a time-averaged clockwise rotating vortex, with a centre at approximately $Y/W = 0.35$ and $Z/H = 0.57$. This is very likely to be one of a pair of counter-rotating vortices.

In near wake of the estate at $X/H = 0.5$, the bounds of the bulk recirculation region is biased toward the upper half of the model. The underbody exit mass flow is high with a large degree of upwash observed, until approximately $Z/H = 0.5$, where the pitch decreases.

Detached flow from the roof induces the downwash observed, most

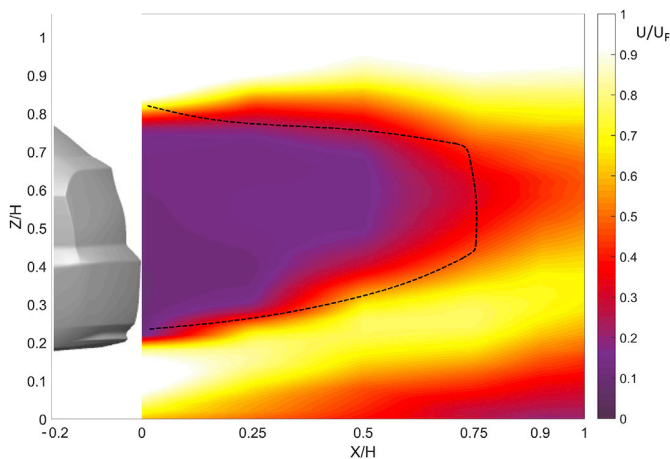


Fig. 21. Streamwise velocity component (U/U_F), the interpolant of results from centreline velocity data available at $X/H = 0, 0.25, 0.5, 0.75, 0.9, 1$. (Region enclosed by vehicle and black dotted line indicates flow with less than 80% data falling within the probe's acceptance cone).

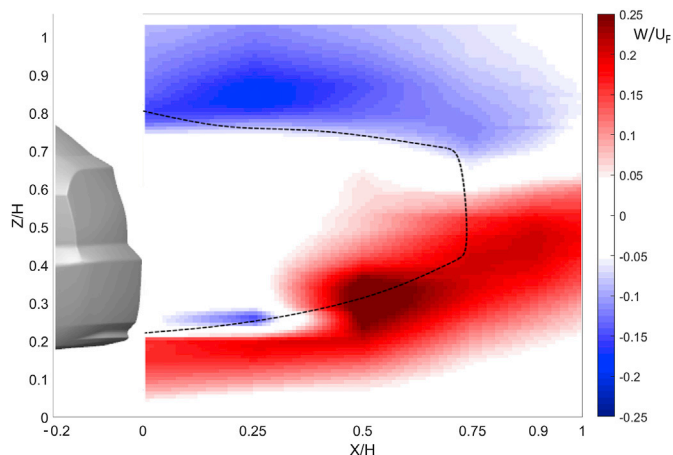


Fig. 22. Vertical velocity component (W/U_F), interpolated from centerline velocity data at $X/H = 0, 0.25, 0.5, 0.75, 0.9, 1$. Region enclosed by vehicle and black dotted line indicates flow with less than 80% data falling within the probe's 45° flow incidence acceptance cone. The data presented within this boundary is considered to be indicative of the wake topology.

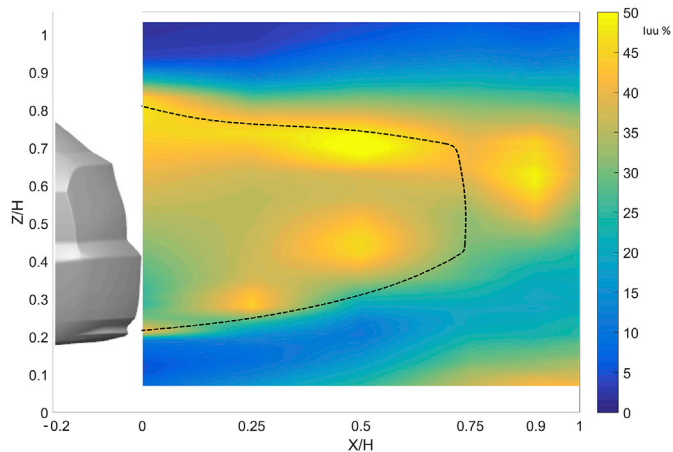


Fig. 23. Streamwise turbulence intensity I_{UU} , the interpolant of results from centreline velocity data available at $X/H = 0, 0.25, 0.5, 0.75, 0.9, 1$. (Region enclosed by vehicle and black dotted line indicates flow with less than 80% data falling within the probe's acceptance cone).

apparent from $Z/H = 0.75$ to 0.9. When compared with the same region of the base pressure contour in Fig. 8, downwash does not coincide with a region of low pressure below the spoiler. This bears a strong resemblance with previous work on the Windsor model (Littlewood et al., 2011), (Littlewood and Passmore, 2012), where the upper vortex in the time-averaged wake is a standalone structure. Littlewood (Littlewood and Passmore, 2012) showed that the Windsor model wake is influenced by upwash from underbody flow and a dominant lower recirculating region present. Similarities also exist between the DrivAer estate (Fig. 8) and Windsor model's base pressure distributions, with a pressure recovery toward the roof of the model.

At the longitudinal distance of $1H$ behind the vehicle, the probes registered a minimum of 95% of flow in the positive streamwise direction. Therefore, the mean recirculation length of the estate vehicle wake is less than $1H$. At this longitudinal position, $X/H = 1$, underbody exit flow is still inducing high upwash with significant momentum ($U_{EXIT,MAX}/U_F = 0.65$). Convergence between the roof downwash and underbody upwash occurs at $Z/H = 0.7$, the likely vertical position of where the wake closes. As with the velocity field at $X/H = 0.5$, there is significant side flow from $Z/H = 0.3$ to 0.5, at the geometric height range

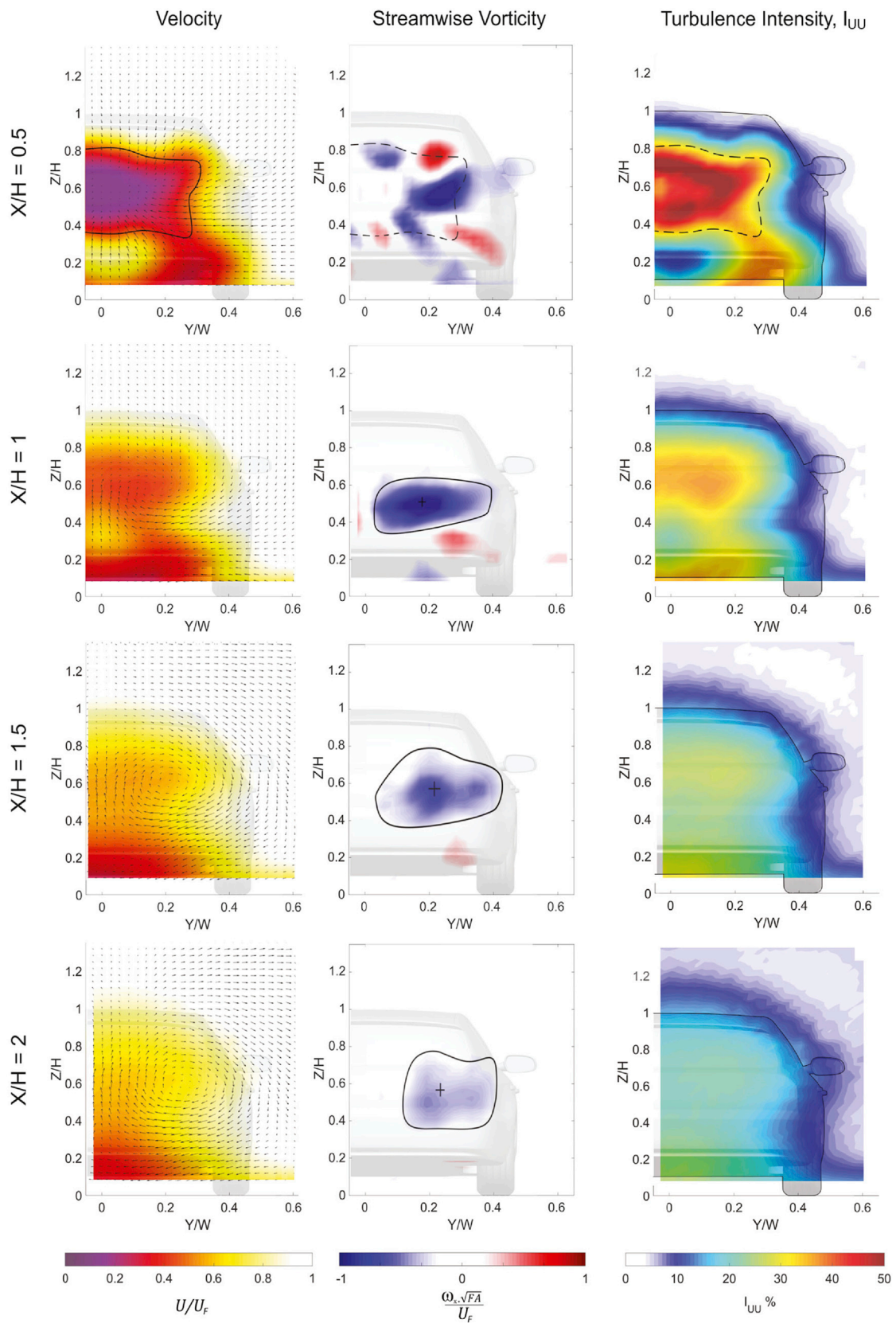


Fig. 24. The time-averaged flow velocities (left), normalised streamwise vorticity (middle) and streamwise turbulence intensity (right) obtained in the transverse planes at the streamwise distances of $X/H = 0.5, 1, 1.5$ and 2. The velocities are coloured by U/U_F , with the projected V and W velocities overlaid. The streamwise vorticity has been normalised by the model's frontal area and freestream velocity. (At $X/H = 0.5$, the region enclosed by vertical axis and black line indicates flow with less than 80% data falling within the probe's acceptance cone).

of the large radius rear bumper.

Progressing downstream to $X/H = 1.5$ and 2 , upwash along the centreline of the vehicle and strong inboard lateral flow at $Z/H = 0.5$ remains present. At these further distances, there is an absence of the accelerated streamwise flow region from the underbody exit flow otherwise noted at $X/H = 0.5$ and 1 . There is little change in the streamwise velocity contours observed from $X/H = 1.5$ to 2 , the wake size increasing from dissipation.

3.6. Turbulence intensity

Fig. 24 (right column) show contours coloured by streamwise turbulence intensity, I_{UU} given by the quotient of standard deviation and mean of the velocity component, expressed as a percentage.

The substantial underbody mass flow has low turbulence, evidence that this is a relatively steady feature of the estate's wake flow. The underbody flow is observed to dissipate and widen progressing downstream, diminished in its presence by $X/H = 2$. The upwash in the underbody exit flow leaves a region of increased turbulence immediately below it, consistent with the observation from the centreline velocity plane data in Fig. 21 that the exit jet remains in form until beyond $X/H = 1$.

The region of high fluctuations are predominantly contained to the upper half of the vehicle. This remains consistent with the observations and proposal that the recirculation region is biased toward the upper half of the vehicle. The large fluctuations have reduced by $X/H = 1$ and diminish further downstream. Strong streamwise flow at $X/H = 0.5$ observed outboard at $Z/H = 0.5$ shows reduced fluctuation and is located further inboard, in contrast to the regions downstream of the wing mirror and wheels. The wing mirror contributes an increase in fluctuations, an effect present further downstream in the wake. The wheel wake is found to be convected inwards and upwards, driven by the diffuser exit flow (Aronson et al., 2000), consistent with earlier rear bumper shear-layer measurements and work by Marklund (Marklund and Lofdahl). The side shear layers are thicker along the entire side of the vehicle and consistent with shear layer measurements indicating a thinner boundary layer leaving the top of the vehicle. The bands of high turbulence towards the bottom of the vehicle are most likely associated with the wheel wake. The wheel wake is observed to convect in towards the centreline of the vehicle at $X/H = 1$ to $Y/W = 0.19$ (from $Y/W = 0.3$ at $X/H = 0.5$). Further downstream, there is some evidence of the fluctuations continuing to be convected inboard to approximately $Y/W = 0.15$ and no longer discernible at $X/H = 2$.

3.7. Streamwise vorticity

Fig. 24 (middle column) show the streamwise vorticity, calculated from the time average velocity field at $X/H = 0.5, 1, 1.5$ and 2 . Vorticity decreases in strength moving downstream. The location of the longitudinal vortex cores and the circulation bounds were found using the Γ_1 and Γ_2 functions (Graftieaux et al., 2001), respectively. The location of the vortex core as outlined in Table 3, and marked by the crosshairs, moves outboard by approximately $0.1W$ over the longitudinal distance of $2H$. Its vertical position is relatively constant within the range of $Z/H = 0.55$ to 0.6 . For the reasons of data being below the acceptable band of quality, the contour plot at $X/H = 0.5$ is solely intended for qualitative

Table 3

Estimated vortex core position given by their lateral location (Y/W) and vertical height (Z/H) at various longitudinal distances (X/H) downstream in the far wake of the vehicle.

X/H	Y/W	Z/H
1	0.19	0.53
1.5	0.22	0.57
2	0.23	0.59

analysis.

The maximum concentration of streamwise vorticity is located behind the tailgate and approximately halfway outboard from the vehicle's centreline. The core location moves upwards and outboard progressing downstream, consistent with the V and W velocity quivers observed from $X/H = 1$ to $X/H = 2$ (Fig. 24). The structures are observed to have a clockwise rotation, influenced and accompanied by the large degree of upwash observed in the wake of the vehicle.

Numerical work by Marklund (Marklund and Lofdahl) also found that a largely symmetric wake still experiencing a larger degree of upwash likewise had a longitudinal pair of vortices with a clockwise rotation. Work on the 25° slant Ahmed body by Wang (Wang et al., 2016) and Vio (Vio et al., 2005) found vortices from underbody upwash flow accounted for approximately 5% of the trailing vortices and that the upwash would mostly decay away by approximately $X/L = 0.15$ (or $X/H = 0.54$).

For the DrivAer, the streamwise vorticity at $X/H = 0.5$ show several different longitudinal vortex structures exist, with lower structures proposed to occur at the rear bumper or wheel arch (counter-clockwise) and wheel/underbody outboard edge still present at $X/H = 1$. The twin longitudinal wheel jet vortices are evident at $X/H = 0.5$, located at $Y/W = 0.28$ and 0.4 , the expected pair with opposite directions of rotation, being convected laterally toward the vehicle's centerline at $X/H = 1$.

Smoke flow visualisation was conducted to understand the origin of the streamwise flow structures present in the vehicle wake, and to elucidate the nature of the recirculation region's vortex system. Fig. 25 shows smoke being injected close to the centerline, parallel to the expected location of entrained inboard flow from a left-right vortex pair. The images are sequenced equally apart, and show the smoke injected travels outboard along the surface of the model's base, diffusing vertically. The vertical stack of smoke splits and the upper section is transported upwards along the rear windscreen. The lower portion of smoke moves downwards, begins to rotate and is convected into the far wake of the model. The rotation is observed to align with the upwash-dominated pair of longitudinal vortices identified from the velocity wake planes.

3.8. Reynolds stress

The normal component of the Reynolds stresses at $X/H = 1, 1.5$ and 2 , presented in Fig. 26, highlight that the separated flow off the top and sides are the regions of largest fluctuations consistent with the locations

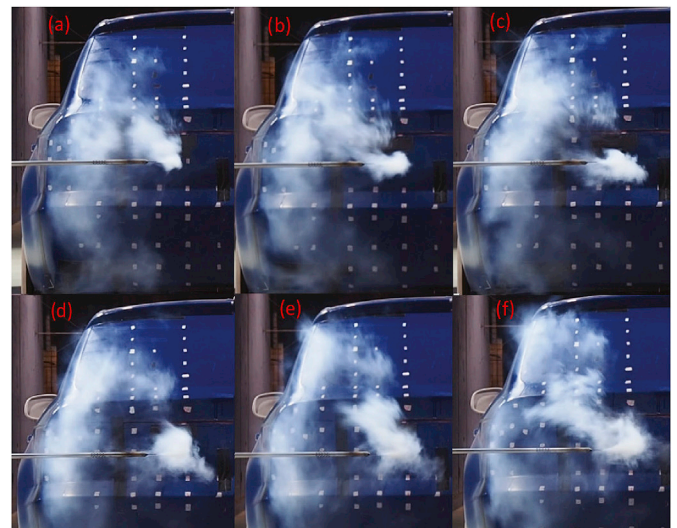


Fig. 25. View of smoke injected parallel to the flow in the recirculation region of the estate. The smoke injected is traced over a sequence of frames extracted from a video, spaced 0.2 s apart (recorded at 25 FPS). The smoke flow visualisation was conducted at $Re_{Length} = 2.4 \times 10^6$.

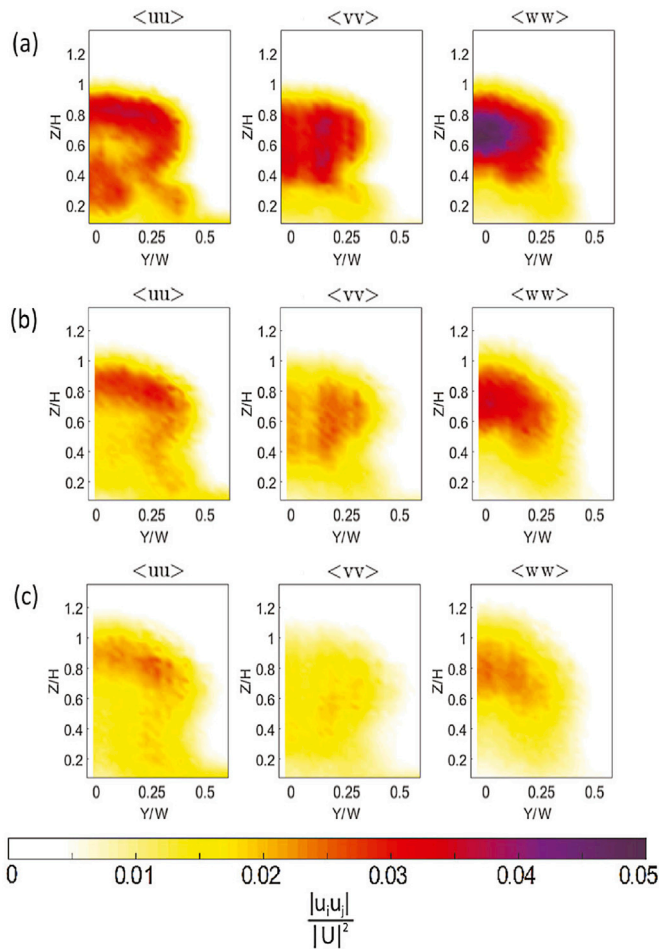


Fig. 26. Normal Reynolds stresses at (from top to bottom) $X/H = 1$ (a); $X/H = 1.5$ (b); $X/H = 2$ (c).

of the shear layers. All three components show the diffusion of unsteadiness, growing vertically and laterally.

The streamwise component, $\langle uu \rangle$, highlights the top and side shear layers unsteadiness at all three locations. At $X/H = 1$, streamwise fluctuations exist for the underbody exit flow which has largely dissipated further downstream. The lateral $\langle vv \rangle$ component shows what may be the downstream turbulence from left-right shedding that would occur. The maximum value of the vertical component $\langle ww \rangle$ is 0.46 at $Z/H = 0.7$ at $X/H = 1$. This suggests the height of the wake closure to be at $Z/H = 0.7$, a convergence point of the vertical fluctuations, associated with a region of highly pitched flow. The large band between $Z/H = 0.6$ and 0.8 comprised of high magnitude vertical stresses also indicates the closure point vertically oscillates and is likely tied to the emission of vortices from the recirculation region, thereby shifting the wake closure point (Duell and George). It is unlikely the underbody exit flow is a large contributor to fluctuations and this shows little evidence of pure vertical unsteadiness at the centreline, below the height of $Z/H = 0.4$ (top edge of rear bumper).

The shear components of the Reynolds stresses at the three longitudinal positions, $X/H = 1, 1.5, 2$ are presented in Fig. 27. As the stresses represent some change in momentum between the two components, the results provide insight into the topology of regions experiencing high shear stresses. The $\langle uv \rangle$ component highlights the influence of various geometries on the side of the estate. The curved radii present on the vehicle's rear bumper ($Z/H = 0.2$ to 0.4) and the D-pillars ($Z/H = 0.6$ to 0.85) correlate with the regions of maximum stress being further outboard rather than the height range of the tail-lamps. The concentration of such $\langle uv \rangle$ stresses are also apparent, with the shear layers off

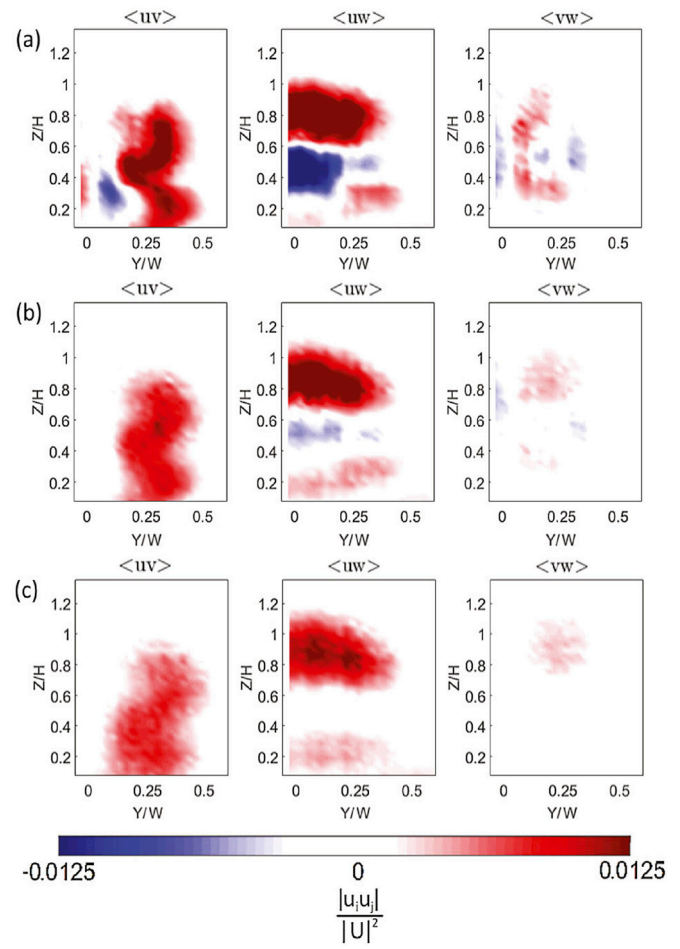


Fig. 27. Shear components of the Reynolds stresses at (from top to bottom): $X/H = 1$ (a); $1X/H = 1.5$ (b); $X/H = 2$ (c).

curved sections diffusing more rapidly with greater spread. The region of underbody exit flow at $Z/H = 0.3$ and $X/H = 1$ changes from a negative shear stress close to the centreline to a positive further outboard.

Regions of high $\langle uw \rangle$ component are related to the upwash and downwash, outlined in the discussion of the time-averaged velocity field results. The stresses approach zero at approximately $Z/H = 0.6$, which is lower than the previously proposed wake closure point at $Z/H = 0.7$. However, the largest positive stresses from the region of downwash diminishes at approximately $0.7H$. This indicates a high gradient in the change in momentum between streamwise and vertical fluctuations, expected at a free stagnation point.

The interaction between lateral and vertical components $\langle vw \rangle$, differ quite substantially from $X/H = 1$ to 1.5 and 2 . In the wake, at the latter distances, there are some stresses which are likely associated with the shedding from the roof spoiler's outboard edge. This indicates that shedding may not be uniform along its entire edge, the $\langle vw \rangle$ plot at X/H showing large stresses present at $X/H = 0.8$ at $Y/W = 0.3$.

3.9. Flow visualisation

Results for the model's front and passenger side window are presented in Figs. 28–31. Flow off the front grille onto the bonnet shows a very short separation zone on the front upper radius, flow beginning to redevelop as it progresses downstream. At the outboard edge of the grille, strong downwash on the lower portion of the grilled spills outboard, rolling up into a longitudinal vortex that is attached to the front and bonnet of the vehicle, its influence evident until approximately two-thirds along the length of the bonnet. Moving outboard, flow detaches

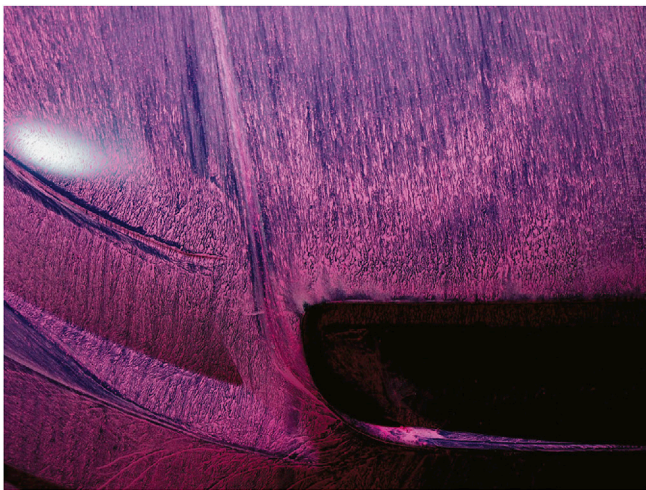


Fig. 28. Surface paint streaklines over the upper grille and headlamps.

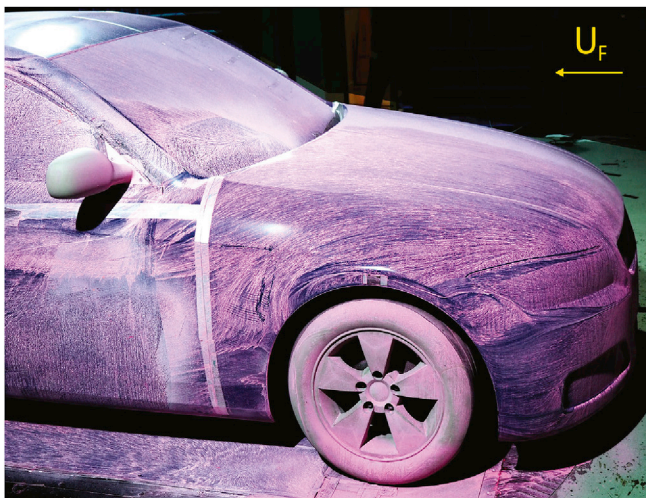


Fig. 29. View from the front right of the model showing the flow over the headlights, wheel arch and front of A-pillar.

off the front bumper rolling into a vortex expanding as it is convected along the headlamp bottom edge. The raised feature line of the headlamp sees a small vortex being formed along the length of its top edge. In Fig. 29, the vortex formed off the top of the front bumper likely detaches when it reaches the outboard edge of the headlamp with no evidence of burst was found on the surface. Around the bumper and over the wheel arch, flow is attached, with separation occurring off the wheel arch's rear onto the side of the body. By the streamwise distance of the A-pillars, flow reattaches onto the side of the body.

Flow over the bonnet in Fig. 30 detaches at the bonnet's edge, stagnating on the surface of the windscreen, at approximately 15% of the windscreen's length in the centerline. A positive bifurcation line is indicated on the figure, differentiating the region of reversed flow down the windscreen.

The A-pillar and passenger window streaklines in Fig. 31 shows the formation of the A-pillar vortex immediately after the side mirror panel's top vertex. The vortex is small in diameter, and follows the bottom edge of the A-pillar. Detached flow off the A-pillar is observed to attach, some distance downstream (indicated by the dashed line). These results compare well with the numerical work of Heft (Heft et al.), where the pressure distribution on the side window and importantly, the formation of the A-pillar vortex correlates with results presented here. The influence of the wing mirror on the passenger window is minimal, the mirror



Fig. 30. View from the front of the model showing the flow over the end of the bonnet, windscreen and front of A-pillar. A dashed line is overlaid showing the positive bifurcation line of stagnation flow onto the rear windscreen.

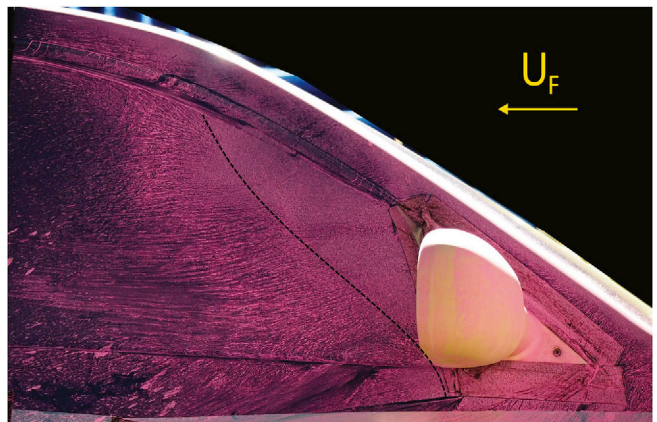


Fig. 31. View from the right side of the model of the A-pillar and side window downstream of the mirror. The dashed line represents the mean reattachment line on the side window.

support and attachment panel likely disturbing the formation of the A-pillar vortex and delaying reattachment onto the side window.

The A-pillar vortex is observed to be formed along the lower edge of the pillar based on the ink streaklines in Fig. 32, results largely symmetric to that of the paint flow visualizations on the opposite side of the vehicle. The clear convergence of ink streaklines upwards in contrast to the other droplets initially influenced by gravity before progressing downstream, is an indication influence the A-pillar vortex exerts on the window surface flow. This vortex structure is observed to be transported onto the outboard roof beam, progressing over the curved surface of the roof beam geometry. No evidence of the A-pillar vortex having an influence on roof surface streaklines were found, suggesting it detaches off the outboard roof beam. Previous numerical results (Heft et al.; Guilmineau, 2014; Jakirlic et al., 2016) also found the A-pillar vortex transported onto the roof, due to the accelerated flow and similarly detaching from the outboard roof beam.

Approaching the rear of the vehicle, surface flow patterns in Fig. 33 show the location of separation at the D-pillars, tail-lights and rear bumper. At the rear bumper, a clear detachment line is not evident, some streaks with sufficient momentum progress around the relatively sharp radius ($r/W_{\text{BUMPER}} \approx 0.13$). Some ink dots are observed to not commence a new streak despite streaklines above and below them had sufficient



Fig. 32. View from the left side of the model of the A-pillars latter portion and side window, downstream of the mirror. Ink streaklines on the bottom edge of the A-pillar are observed to initially be transported along the roof beam's lower edge. ink droplets placed above the rear passenger window are associated with the A-pillar vortex structure being transported onto the roof, once the A-pillar vortex structure moves past the vehicle's B-pillar.

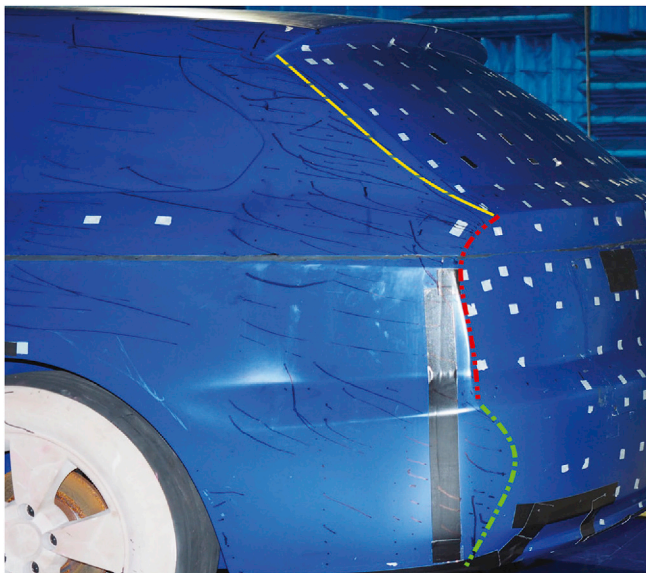


Fig. 33. View of the D-pillar, rear tail-light and rear bumper and from the left side of the vehicle. The red and green and translucent yellow lines represent the furthest downstream location where flow detachment occurs. (For interpretation of the references to colour in this figure legend, the reader is referred to the Web version of this article.)

momentum to progress further downstream. Whilst the error arising from the inertia of ink droplets are a factor, the curved bumper, non-trivial upstream boundary layer conditions (as a result of reattached flow from the rear wheel and wheel arch) are likely to influence the nature of the separation (Buresti et al., 1997). Based on the mean and standard deviation pressure distributions from Figs. 8 and 9, the flow off the bumper is likely very unsteady, changes to the location of separation are the cause of very low base pressures with a high degree of fluctuations.

Flow at the tail-lights and bottom of the D-pillar separate at the sharp edge of the tail-light geometry. Of interest, flow at the bottom of the D-pillar is attached, being the apposite source of the strong lateral inboard flow observed in the $X/H = 0.5$ wake velocity plane (Fig. 24). The sharp separation point at the tail-lights additionally matches the sharp rise in streamwise turbulence intensity and low degree of lateral inboard flow found in the side shear layer measurements $Z/H = 0.5$ (Fig. 14).

At the D-pillar, the flow separation along its length is not apparent, similar to the conditions observed at the bumper, although flow approaching the D-pillar is considered to be steady. Flow begins to detach at the start of the D-pillar radius (translucent yellow line), the ink streaklines moving down the D-pillar expected to be wet droplets under some influence of gravity.

3.10. Time-averaged wake structure

The shape of the time-averaged wake recirculation structure is of interest, similar wakes have been identified as being a torus (Volpe et al.), or a horseshoe system (Venning et al.; Aljure et al., 2014). Results from the base pressure study found the lower structure was dominant, significant lateral inflow coming from the base of the D-pillars and the streamwise component of the normal Reynolds stresses coming inboard at approximately $Z/H = 0.5$. No clear evidence of a torus-shaped region of the unsteadiness apparent in the $\langle uu \rangle$ Reynolds stress component in the lower region shows a band of reduced fluctuations that is not consistent with a torus system.

Results from the smoke flow visualisation are indicative that a toroidal system often found on square-back bodies such as the Ahmed may not exist. The splitting of the smoke stream at the base of the vehicle and subsequent rotation of the lower smoke stream portion provides some evidence that the time-averaged recirculation structure is comprised of a lower and upper horseshoe system whose legs are pointed and therefore extend in the streamwise direction. Although the results can be subjective when being interpreted, this sequence of images presented was observed on multiple occasions. However, the sensitivity of the smoke injection location may likely change what is observed depending on the seeding location, potentially changing the perceived strength of the flow patterns observed.

The exact nature is still to be determined, if such a lower horseshoe vortex may bear similarities to that of the ASMO vehicle (Aljure et al., 2014), albeit flipped vertically. The lower vortex would approach closer to the body as it moves outboard, turns vertical at the tail-lights and is twisted to point downstream. This horseshoe vortex would additionally maintain the same direction for circulation as the longitudinal vortices observed in the far wake. Venning et al. (Venning et al.) found the horseshoe structures increased the circulation of longitudinal vortices off a slant surface being convected into the wake. With streamwise structures of the same rotational direction being convected from the underbody, a horseshoe wake system would contribute to the increased circulation of such structures. However, further work is required to be confident in this speculative characterisation of this structure.

The wake was found to be largely symmetric, with small degrees of asymmetry expected to exist from model positioning, flow straightness or model imperfections. The mean pressure distribution quantities (see Figs. 8 and 9) and tracking of the horizontal pressure gradient indicates the wake's influence at the model's base to be largely symmetric. Moreover, flow visualisation results found the wake and general flow-field around the rest vehicle (Figs. 31 and 32) to be similar, suggesting the vehicle's large scale flow structures to be similar.

4. Conclusions

An investigation in the velocity flow field and base pressure distribution on a full-scale realistic generic estate vehicle has been experimentally conducted in a wind tunnel. The comprehensive data provides a basis on which to evaluate and correlate future studies into this important and popular estate geometry. These results are intended to form the basis on which to further study the unsteady nature of the estate near wake, with specific consideration of active and passive flow control devices. Additionally, these results will be used in parallel ongoing reduced Reynolds number and full-scale experiments, to measure reversed flow quantities and better understand the transient nature of the wake.

At the operational range of a full-scale vehicle where aerodynamic

losses are significant, the effect of Reynolds number has minimal influence on the drag. The subsequent wake velocity field experiments were conducted at $Re_{Length} = 8 \text{ M}$.

The base pressures on the DrivAer estate show a region of minimum pressures at the lower half of the body with a general pressure recovery towards the centerline of the vehicle. Base pressures along the centerline confirm the lower half of the body experiences the minimum pressures. Pressure recovery is present on the rear windscreen surface, increasing towards ambient pressure on the underside of the roof spoiler. A sharp drop in pressure on the underside and tip of spoiler indicates separation from the roof trailing edge radius.

Velocity fields show substantial momentum of a steady nature exiting from the smooth underbody diffuser and induces a large component of upwash into the wake. Strong lateral flow around the radiused rear bumper and D-pillar of the estate are also present. Downwash from flow off the roof spoiler is present, but the underbody exit flow's upwash is more dominant. Convergence of pitch and streamwise data collected by the velocity probe indicate the recirculation length is approximately $0.75H$ behind the model ($X/L \sim 0.24$), generally found to be shorter than simplified geometries as well as located at approximately 62% of the vehicle height.

Time-averaged longitudinal vortices are present in the far wake consistent with previous findings on tapered square-back bodies and other estates. These longitudinal structures are have a clockwise rotation in contrast to sedan type vehicles, a result of the large upwash observed for the estate wake. Reynolds stresses highlight streamwise unsteadiness of the underbody exit flow, a recirculation point that moves vertically as well as top and side shear layers that are quite turbulent.

The flow structures at the front of the vehicle have been described with the assistance of flow visualisation results, previously unavailable through existing literature. Results illustrate complex flow features as a consequence of operational requirements for vehicles. Regions of stagnation, separation or reattachment, and the formation of vortex structures, have been identified with the their influences on the wake noted where applicable.

A topological time averaged flow field and flow over an estate has been described and proposed. This would consist of a dominant lower vortex that is likely to form a trailing half horseshoe structure and an upper vortex system that forms from rolling up of shear layer instabilities off the roof and D-pillar region. Flow on the rear windscreen or backlight in turn moves up vertically and outboard away from the centreline. Separation points on curved features inclusive of the rear bumper and D-pillar are not fixed in location.

Acknowledgements

The authors would like to thank the Ford Motor Company for access to the full-scale model used in this experimental study and communication of results for the rolling road study.

References

- S. Ahmed, G. Ramm, G. Faltin, Some salient features of the time-averaged ground vehicle wake, SAE Technical Paper Series.
- Aljure, D., Lehmkühl, O., Rodríguez, I., Oliva, A., 2014. Flow and turbulent structures around simplified car models. *Comput. Fluids* 96 (3), 122–135.
- Aronson, D., Brahim, S.B., Perzon, S., 2000. On the Underbody Flow of a Simplified Estate. Report. SAE Technical Paper.
- Ashton, N., Revell, A., 2015. Comparison of RANS and DES Methods for the DrivAer Automotive Body. Report. SAE Technical Paper.
- Bell, J., Burton, D., Thompson, M., Herbst, A., Sheridan, J., 2016. Dynamics of trailing vortices in the wake of a generic high-speed train. *J. Fluid Struct.* 65, 238–256.
- Bell, J., Burton, D., Thompson, M., Herbst, A., Sheridan, J., 2016. Flow topology and unsteady features of the wake of a generic high-speed train. *J. Fluid Struct.* 61, 168–183.
- T. Blacha, M. Islam, The aerodynamic development of the new Audi Q5, SAE Int. J. Passeng. Cars 10(2).
- Bonnnavion, G., Cadot, O., Evrard, A., Herbert, V., Parpais, S., Vigneron, R., Déleroy, J., 2017. On multistabilities of real car's wake. *J. Wind Eng. Ind. Aerod.* 164, 22–33.
- A. Brunn, E. Wassen, D. Sperber, W. Nitsche, Active Drag Control for a Generic Car Model, Springer.
- Buresti, G., Fedeli, R., Ferraresi, A., 1997. Influence of afterbody rounding on the pressure drag of an axisymmetrical body. *J. Wind Eng. Ind. Aerod.* 69, 179–188.
- Cogotti, A., 1998. A Parametric Study on the Ground Effect of a Simplified Car Model. Report.
- C. Collin, S. Mack, T. Indinger, J. Mueller, A numerical and experimental evaluation of open jet wind tunnel interferences using the DrivAer reference model, SAE Int. Journal of Passenger Cars 9(2).
- Croll, R., Gutierrez, W., Hassan, B., Suazo, J., Riggins, A., 1996. Experimental Investigation of the Ground Transportation Systems (GTS) Project for Heavy Vehicle Drag Reduction. Report. SAE Technical Paper.
- Crouch, T., Burton, D., Brown, N., Thompson, M., Sheridan, J., 2014. Flow topology in the wake of a cyclist and its effect on aerodynamic drag. *J. Fluid Mech.* 748, 5–35.
- E. G. Duell, A. George, Experimental study of a ground vehicle body unsteady near wake, SAE International.
- Federal Chamber of Automotive Industries, 2017. SUV Sales Overtake Passenger Cars for First Time Ever.
- Fletcher, C., Barbuto, J., 1986. Flow behaviour in rearward-facing cavities. *Appl. Math. Model.* 10, 176–184.
- Fourrie, G., Keirsbulck, L., Labraga, L., Gillieron, P., 2011. Bluff-body reduction using a deflector. *Exp. Fluids* 50, 385–395.
- Grafteaux, L., Michard, M., Grosjean, N., 2001. Combining PIV, POD and vortex identification algorithms for the study of unsteady turbulent swirling flows. *Meas. Sci. Technol.* 12 (9), 14–22.
- Grandemange, M., Gohlke, M., Cadot, O., 2013. Turbulent wake past a three-dimensional blunt body. part 1. global modes and bi-stability. *J. Fluid Mech.* 722, 51–84.
- Grandemange, M., Cadot, O., Courbois, A., Herbert, V., Ricot, D., Ruiz, T., Vigneron, R., 2015. A study of wake effects on the drag of ahmed's squareback model at the industrial scale. *J. Wind Eng. Ind. Aerod.* 145, 282–291.
- Guilmineau, E., 2014. Numerical simulations of flow around a realistic generic car model. SAE Int. J. Passeng. Cars 7 (2), 646–653.
- Heft, A.I., Indinger, T., Adams, N., 2012. Introduction of a New Realistic Generic Car Model for Aerodynamic Investigations, Report. SAE International.
- A. Heft, T. Indinger, N. Adams, Experimental and numerical investigation of the DrivAer model, in: Proceedings of the ASME 2012 Fluids Engineering Summer Meeting.
- A. Heft, T. Indinger, N. Adams, Investigation of unsteady flow structures in the wake of a realistic generic car model, in: 29th AIAA Applied Aerodynamics Conference.
- Jakirlic, S., Kutej, L., Hanssmann, D., Basara, B., Schutz, T., Tropea, C., 2016. Rear-end shape influence on the aerodynamic properties of a realistic car model: a rans and hybrid les/rans study. In: Dillmann, A., Heller, G., Kramer, E., Wagner, C., Breitsamter, C. (Eds.), *New Results in Numerical and Experimental Fluid Mechanics X: Contributions to the 19th STAB/DGLR Symposium Munich, Germany, 2014*. Springer International Publishing, pp. 397–407.
- A. Kabanovs, G. Hodgson, A. Garmory, M. Passmore, A. Gaylard, A parametric study of automotive rear end geometries on rear soiling, SAE Int. J. Passeng. Cars - Mech. Syst. 10(2).
- Kahlighi, B., Jindal, S., Iaccarino, G., 2012. Aerodynamic flow around a sport utility vehicle - computational and experimental investigation. *J. Wind Eng. Ind. Aerod.* 107, 140–148.
- Kremheller, A., 2014. The Aerodynamics Development of the New Nissan Qashqai. Report. SAE Technical Paper.
- Lienhart, H., Stoots, C., Becker, S., 2002. Flow and Turbulence Structures in the Wake of a Simplified Car Model, *New Results in Numerical and Experimental Fluid Mechanics 3*, pp. 323–330.
- Littlewood, R., Passmore, M., 2012. Aerodynamic drag reduction of a simplified squareback vehicle using steady blowing. *Exp. Fluids* 53, 519–529.
- Littlewood, R., Passmore, M., Wood, D., 2011. An investigation into the wake structure of square back vehicles and the effect of structure modification on resultant vehicle forces. *SAE Tech. J. Engin.* 4 (2), 29–37.
- J. Marklund, L. Lofdahl, Influence of a Diffuser to the Wake of a Passenger Car, ASME.
- McArthur, D., Burton, D., Thompson, M., Sheridan, J., 2016. On the near wake of a simplified heavy vehicle. *J. Fluid Struct.* 66, 293–314.
- D. McArthur, D. Burton, M. Thompson, J. Sheridan, Development of a wind tunnel test section for evaluation of heavy vehicle aerodynamic drag at a scale of 1:3, SAE Int. J. Comm. Vehicles 6(2).
- E. Mercker, K. Cooper, A Two-measurement Correction for the Effects of a Pressure Gradient on Automotive, Open-jet, Wind Tunnel Measurements, SAE International.
- Mousley, P., 2011. Tfi - Dynamic Pressure Measurement System. URL: <http://www.turbulentflow.com.au/Downloads/DynamicPressureMeasurementSystem.pdf>.
- Mousley, P., 2011. Flyer_cobraprobe. URL: http://www.turbulentflow.com.au/Downloads/Flyer_CobraProbe.pdf.
- A.-K. Perry, G. Pavia, M. Passmore, Influence of short rear end tapers on the wake of a simplified square-back vehicle: wake topology and drag, *Exp. Fluids* 57(169).
- Strangfeld, C., Wieser, D., Schmidt, H., Woszidlo, R., 2013. Experimental Study of Baseline Flow Characteristics for the Realistic Car Model DrivAer. Report.
- J. Venning, D. LoJacono, D. Burton, M. Thompson, J. Sheridan, The nature of the vortical structures in the near wake of the ahmed body, *J. Automob. Eng.* 231.
- Vino, G., Watkins, S., Mousley, P., Watmuff, J., Prasad, S., 2005. Flow structures in the near-wake of the Ahmed model. *J. Fluid Struct.* 20, 673–695.
- R. Volpe, P. Devinant, A. Kourta, Unsteady Experimental Characterization of the Natural Wake of a Squareback Ahmed Model, ASME.
- Wang, H., Zhou, Y., Zou, C., He, X., 2016. Aerodynamic drag reduction of an Ahmed body based on deflectors. *J. Wind Eng. Ind. Aerod.* 148, 34–44.

- Wieser, D., Schmidt, H., Mäüller, S., Strangfeld, C., 2014. Experimental comparison of the aerodynamic behavior of fastback and notchback DrivAer models. *SAE Int. J. Passeng. Cars* 7 (2), 682–691.
- Wittmeiere, F., Kuthada, T., 2015. Open grille DrivAer model - first results. *Int. J. Passeng. Cars* 8 (1), 252–260.
- Xia, C., Shan, X., Yang, Z., 2016. Comparison of different ground simulation systems on the flow around a high-speed train. *J. Rail Rapid Trans.* 0, 1–13.
- Yazdani, R., 2015. Steady and Unsteady Numerical Analysis of the DrivAer Model - Thesis.